Observed scales of short-lived nocturnal turbulent structures

R.B. Schulte

Master Thesis Geoscience & Remote Sensing

Date: 4 July 2017

TU Delft

Observed scales of short-lived nocturnal turbulent structures

by

R.B. Schulte

to obtain the degree of Master of Science
at the Delft University of Technology,
to be defended publicly on Wednesday July 12, 2017 at 14:00 PM.

T̃U Delft

Abstract

Nocturnal weather can have significant impact on society. Dangerous conditions can occur during or after clear sky nights with weak winds. The lack of turbulent mixing during these nights can cause the near-surface temperature to rapidly decrease. This can lead to fog or sever frost, which can affect, for example, traffic safety as a result of reduced visibility or road frost.

A single short-lived turbulent event can renew turbulent mixing and hamper/stop the formation of fog or severe frost, averting the aforementioned dangerous conditions. Short-lived turbulence has been studied using single tower observations, but the spatial scale of this phenomenon is not yet known. The goal of this study is to fill that gap and estimate the spatial scale of short-lived turbulent structures in the nocturnal boundary layer.

Short-lived turbulent structures are studied using wind speed and near-surface temperature observations from two existing observational networks in the Netherlands. Nights with short-lived turbulence are selected using an automated filter and manual selection. For each network, a particular selection is studied, containing about 10 nights. Visual analysis is first used to identify that the turbulent structures span multiple stations of the network. If so, the correlation between pairs of stations is quantified as a function of their spatial separation. Next, an exponentially decaying fit is applied to this data. The e-folding distance of this fit serves as the estimation of the spatial scale of the turbulent structure.

First the automated weather station network of the KNMI is studied, with 32 stations spanning the Netherlands. Visual analysis of the network observations shows that the structures are too small to be captured by the network, with its stations being 30 km apart on average. Hence, the intermediate conclusion is drawn that a denser network is required to estimate the spatial scale of the short-lived turbulent structures.

Such denser network is found by using the observational masts at and around Schiphol Airport. Visual analysis shows that this network is sufficiently dense for the turbulent structures to span multiple stations. Using the aforementioned methodology, the scales of the short-lived turbulent structures are estimated to range between 1.5 km and 24 km, with a median of 9 km. The spatial scale of short-lived turbulent structures is therefore estimates at 9 km.

This study should be considered to be a first-order estimate. In fact, one of the weaknesses of the method used is that it only takes the distance between stations into account (without incorporating directional effects). As such, it assumes the turbulent event to be spatially isotropic. At present, limitations by the Schiphol Airport network do not allow for a clear assessment of the spatial structure of the events.

To accurately study both the dynamics and the spatial coherence of short-lived turbulent structures, a dense and uniformly distributed network is recommended. Ideally, such set-up would consist of a nested fine-scale network within a courser network which needs to span a distance of 25 km minimum to capture turbulent events such as the ones studied here.

In addition to turbulent events, regional temperature variations are found in the Schiphol Airport network observations. Near-surface temperature differences up to 9^oC over a distance of 40 km are observed during nighttime. The daytime temperature at these stations is nearly identical, stressing the differences in atmospheric physics during day and night. These local variations may result from different local (soil) conditions, local turbulence and clouds. Artificial turbulence, caused by large airplanes taking off, is observed close to the airport's runways, increasing the local near-surface temperature up to 4^oC. It will be interesting to also study the impact of artificial turbulence on the near-surface temperature as a follow up of the current work.

Contents

1

Introduction

Nighttime weather can have a large impact on society. On nights with a clear sky and weak wind, the surface can cool rapidly, which can lead to fog or frost formation. The reduced visibility from fog can lead to problems for air traffic and can cause very dangerous situations for road traffic. The largest chain collision in Dutch history, a collision near Breda in 1990 involving over a hundred vehicles and killing 8 people [1], was a result of sudden development of thick fog. A rapid decrease in temperature can also lead to severe frost, which can cause dangerous situations, like freezing rain. It can also result in significant financial damages. For example, severe frost on the night of the 19th and the 20th of April 2017, destroyed a significant part of the crops of fruit farmers in Europe, resulting in a significant price increase for apples in the Netherlands [2]. The complicated interactions between various processes in the lower nocturnal atmosphere are still not fully understood and an accurate prediction of these potentially dangerous conditions is difficult. For that reason, more research on the atmospheric boundary layer (ABL) during the night is necessary. This study focuses on short-lived turbulence in the nocturnal ABL, which can have a significant impact on the near-surface temperature.

---

[1] http://www.zero-meridean.nl/i_breda_061190.html
[2] http://nos.nl/artikel/2175077-appels-dit-jaar-fors-duurder-door-slechte-oogst.html
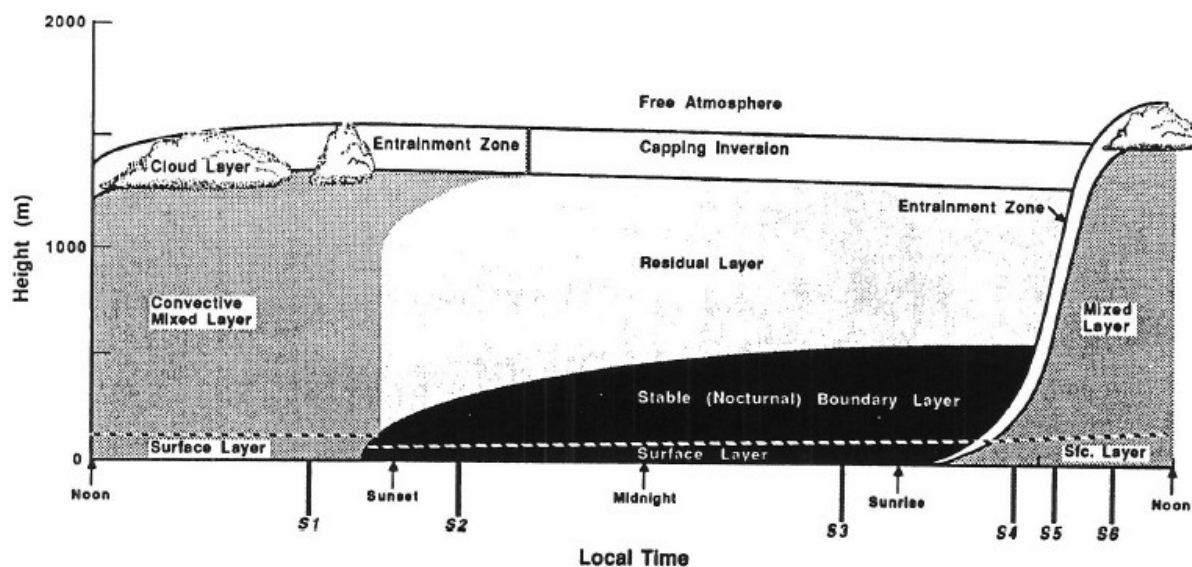
Figure 1.1: A schematic diagram of the diurnal cycle of the ABL. A very turbulent mixed layer is found during the day. Rising thermals of warm air from the surface generate strong turbulence and result in a boundary layer height of approximately 1 km. During the night, the convective mixed layer transitions to the less-turbulent residual layer and the stable boundary layer with a height of about 100 m and very little turbulence. Figure from *Stull 1988*, figure 1.7.

Figure 1.2: A typical time series of temperature in the regimes of the stable boundary layer. There is a weak temperature decrease (red) in the weakly stable regime and an equilibrium is reached quickly. Strong stratification is found in the very stable regime, because cold air at the surface does not mix with the warm higher layers. This allows the temperature (blue) to decreases strongly and it takes a long time to find a new equilibrium. In between these two regimes, short-lived turbulence is found which can temporarily increase the temperature (green). [*Van de Wiel 2016*]

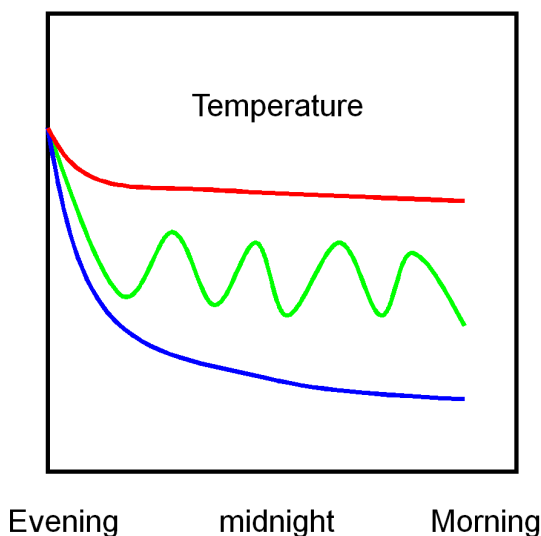The ABL is the lower layer of the atmosphere that is affected by the diurnal cycle. Its behaviour is very different during nighttime compared to daytime, as can be seen in figure 1.1. The dynamics of the daytime ABL is familiar to most. Solar radiation heats the surface, which in turns heats the adjacent air. These warmer, more buoyant, air parcels form rising thermals, forming a convective ABL with strong turbulent mixing and an ABL height of approximately 1 km. During the night, the sun does not heat the surface and it starts to cool as a result of radiative cooling, i.e. cooling by emission of long wave radiation (heat). Without the rising thermals, the boundary layer transforms into a stable boundary layer (SBL) with a height of a approximately 100 m, shown in figure 1.1 [*Stull 1988*].

Radiative cooling in the SBL causes stratification which suppresses turbulence. The cool air near the surface is less buoyant and it therefore tends to stick to the surface. Energy is needed to overcome this effect and mix the cold air with the warmer, more buoyant, air aloft. Consequently, the SBL has very little turbulent mixing compared to the daytime ABL. The energy required to sustain turbulence can come from wind shear, i.e. the difference in wind speed or direction over a relatively short vertical distance. External factors, e.g. clouds or synoptic changes, can also impact the stability of the atmosphere. However, without external factors it depends on the wind shear if turbulence is sustained during the night or not.

In literature, generally two SBL regimes are distinguished: the weakly stable boundary layer (WSBL) and the very stable boundary layer (VSBL) [*Mahrt 1999, Mahrt et al. 1998, Monahan et al. 2015, Van Hooijdonk et al. 2015, 2016*]. A typical evolution of the near-surface temperature of these two regimes can be found in figure 1.2. The main distinction between the two is that the WSBL is continuously turbulent where the VSBL is not [*Mahrt et al. 1998*]. Without turbulent mixing in the VSBL, the near-surface temperature can decrease rapidly until a balance is reached, as shown in blue in figure 1.2. This can lead to formation of frost or, when the temperature reaches the dewpoint temperature, to fog, leading to the aforementioned dangerous situations. An exemplary picture of the VSBL is shown in figure 1.3.

While the two regimes of the WSBL and VSBL are quite well defined, there are also cases where turbulence is sustained for only a limited period of time. These short-lived turbulent events reignite the mixing of warmer air aloft with the cold air near the surface, resulting in an increase in the near-surface temperature. A typical response of increasing temperature with intermittent turbulent events is shown in green in figure 1.2. When such a turbulent event occurs at the right time, the associated mixing can stop the formation of fog and/or prevent severe frost, averting dangerous or damaging weather conditions.

There are multiple studies on short-lived nocturnal turbulence, generally referred to as intermittent turbulence. Nearly all observational studies focus on temporal occurrences of intermittent turbulence, often using observations from a single location [*Acevedo et al. 2006, Nakamura and Mahrt 2005, Salmond 2005, Sun et al.*

Figure 1.3: An example of the VSBL, just before sunrise at Kinderdijk, the Neherlands. The picture shows very few high altitude clouds, very weak winds and weak fog formation, which is typical for the VSBL. By Mark Leeman[3].

2002, 2012, Van de Wiel et al. 2003, Weber and Kurzeja 1991]. An interesting exception is the study by *Coulter and Doran 2002*, who also studied the spatial occurrences of intermittent turbulence. Unfortunately, this study was limited to observations at only three locations with a relative distance in the order of 20 km.

Other studies aimed to simulate intermittent turbulence in the atmosphere. These studies are essential to understand the mechanisms that generate turbulence [*Van de Wiel et al. 2002a,b*] and they can show that intermittency is intrinsic to the SBL [*Ansorge 2016, Ansorge and Mellado 2014, He and Basu 2015*]. While simulations play a very important role in the research on intermittent turbulence, one must keep in mind that they simulate idealized and simplified conditions.

While the impact of a short-lived turbulent event can be significant, previous studies on intermittency do not yet provide an answer to the horizontal scale at which these events are found in nature. It is yet unknown if these events are very small and only have a local effect, or if they affect a large region. This study aims to fill that gap by giving a first estimate of the horizontal scale of short-lived turbulent events, based on observations from multiple locations in the Netherlands.

The Netherlands is a relatively small country in Western Europe at the North Sea, sharing borders with Germany (east) and Belgium (south). The country is geographically very low and flat and is partly located in the river delta of three major rivers: the Rhine, the Meuse and the Scheldt. With an average population density of over 500 people per km^2 of land, in 2016, it is classified as a very densely populated country [4].

The flat geography makes the Netherlands a very suitable location to study the SBL. For example, in the absence of irregular topography (e.g. hills and valleys), drainage flows and other local circulations are unlikely to occur [*Martínez et al. 2010, Monti et al. 2002, Román-Cascón et al. 2015*]. Another reason to study short-lived turbulence in the Netherlands is that, due to time limitations, and existing observational network is required for this study. The Royal Netherlands Meteorological Institute (KNMI) owns and maintains a very dense observational network of 35 stations spread over the Netherlands, as well as the Cesar Observatory, a 200 m high measurement tower which has proven to be a very valuable tool in SBL research [*Nieuwstadt 1984, Van de Wiel et al. 2012, Van Hooijdonk et al. 2015, 2016*].

The Netherlands appears to be well suited form an infrastructural perspective, but it may not necessarily be suitable from a physical perspective. While stable conditions with short-lived turbulent structures are observed in the Netherlands, these conditions are expected to be uncommon. The weather can be quite

---

[3]http://fotoblog.markleeman.nl/
[4]http://statline.cbs.nl/Statweb/publication/?VW=T&DM=SLNL&PA=37296ned&D1=68&D2=0,10,20,30,40,50,(l-1)-l&
 HD=170615-1035&HDR=G1&STB=T

variable, clouds and rain are common throughout the year and it is hard to predict the weather for long periods of time. One also has to keep in mind that the heterogeneity of the geography, due to the many cities, towns, farmland and forests resulting from the high population density, might result in local differences [*Steeneveld et al. 2011*]. However, in order to give a first estimate of the horizontal scale of the short-lived turbulent structures, a small number of suitable nights is expected to be sufficient.

The main objective of this study is to determine the horizontal scale at which short-lived turbulent structures occur in the stable boundary layer. It focusses on turbulence that is intrinsic to the SBL as was proven by simulation studies. It will provide a first estimate of the scales at which these structures are found in observations in the Netherlands. The project will serve as a proof of concept for further research on this topic. The knowledge gained from this research on the retrieval of intermittent turbulence and the scale of the phenomenon will contribute to the design of future observational campaigns on the subject. This objective, together with the scope of the project, leads to the following research questions (RQ):

> RQ 1 *Can short-lived turbulent structures in the nocturnal boundary layer be observed using existing observational networks?*
>
> RQ 2 *If so, what is the spatial scale of short-lived turbulent structures in the nocturnal boundary layer?*
>
> RQ 3 *What network design is required for an in-depth study of short-lived turbulent structures in the nocturnal boundary layer?*

A number of preparatory steps are required to answer the research questions. These steps are represented by the following research sub-questions (RsQ):

RsQ 1 *What are the meteorological conditions in which short-lived turbulent structures are found and how can it be applied to case selection?*
Understanding the conditions in which the phenomenon occurs is required to identify nights that are suitable to study. This theoretical knowledge needs to be translated to observable criteria in order to select nights with short-lived turbulent events.

RsQ 2 *What meteorological parameters are best suited to observe short-lived turbulence using existing observational networks?*
This study requires observations from existing networks and is therefore limited in the instruments that are available. It is important to use meteorological parameters that are relatively cheap and easy to measure, while it is still possible to observe the turbulent events.

RsQ 3 *How can the scale of the turbulent structure be estimated form the data of the observational network?*
A methodology needs to be developed to analyze the data of the observational network and derive a measure for the scale of the turbulent structures.

RsQ 4 *Are the proposed methods valid in estimating the spatial scale of short-lived turbulent structures?*

RsQ 5 *What are the limitations of the existing networks when studying short-lived turbulent structures?*
Existing networks are used to study short-lived turbulent structures, which are designed for a different purpose. By knowing the weaknesses of the networks which were used in this study, recommendations can be made for future networks to study short-lived turbulence.

This report is set up in six chapters, including this introduction chapter. The second chapter describes the theory required to understand the conditions in which short-lived turbulent structures are found. It discusses the surface energy balance, turbulence and boundary layer stability. Chapter 3 describes the methodology of this study, including the observational networks, the case selection procedure, the correlation between near-surface temperature and wind speed, and the analysis methods to find the scale of the structures. Chapter 4 describes and discusses the results of the analysis of the network of operational weather stations in the Netherlands. Chapter 5 describes and discusses the results of a denser network around Schiphol Airport. The study ends with chapter 6 where the conclusions and recommendations for the future are presented.

2

Theoretical background

Conditions where short-lived turbulent events can be found are already briefly discusses in chapter 1. This chapter goes into more detail of these boundary layer conditions. A brief theoretical background is given on the meteorological concepts used in this study. The topics are limited to concepts of boundary layer stability and the conditions in which short-lived turbulence is found. It purposely does not go into detail on possible causes of intermittent turbulence, in order to study the observations without prior expectations of the outcome.

The aim of this chapter is to understand the principles of (short-lived) turbulence and boundary layer stability. The knowledge gained is applied throughout the whole study, but is of particular interest during the case selection process (section 3.3), where nights with short-lived turbulent events are selected.

This chapter starts with a description of the surface energy balance, which is followed by an introduction to turbulence. Next the concept of buoyancy is discussed, leading to the final section in which the concept of boundary layer stability is discussed.

2.1. Surface energy balance

The state of the boundary layer is heavily affected by processes occurring at the land surface, e.g. differential heating, evaporation and resulting cloud formation, and heat exchange between the soil and atmosphere. An understanding of the energy exchange between the Earth's surface and the atmosphere is required to understand the stability of the boundary layer.

The surface energy balance equation is given by

$$Q = H + L_v E + G, \tag{2.1}$$

where Q is the net radiation, H the sensible heat flux, $L_v E$ the latent heat flux and G the soil heat flux. Q is defined positive when directed *towards* the surface. The heat fluxes are defined positive when directed
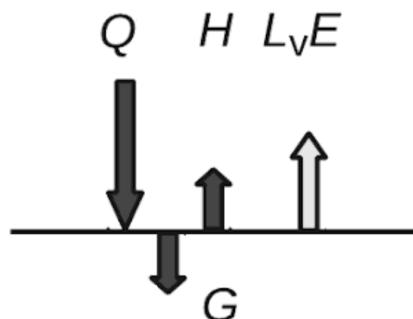

Figure 2.1: The surface energy balance describing the transport of energy during daytime. Q, the net radiation, represents solar radiation heating the surface, G the soil heat flux storing heat in the soil, H the turbulent heat flux cooling the surface and $L_v E$ the latent heat flux cooling the surface through evapotranspiration. Figure from *Moene and Van Dam 2014*, figure 1.7.
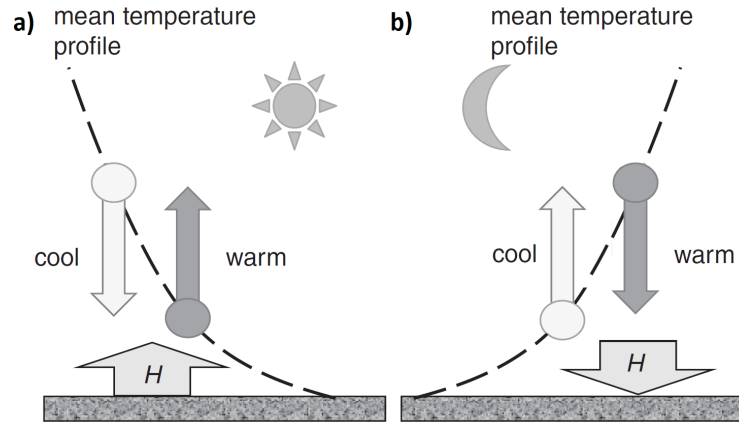
Figure 2.2: Sketch of turbulent heat transport and its relation to surface flux H for both daytime (a) and nighttime (b). The dashed line represents the mean temperature profile. During daytime, turbulent mixing brings cold air to the surface and warm air to higher altitudes; cooling the surface. During the night, the temperature profile changes and turbulent mixing moved warmer air from higher up towards the surface and pushes cool air upwards; heating the surface. Original figure from *Moene and Van Dam 2014*, figure 3.5.

away from the surface. The main advantage of using a surface is that it has no volume. Therefore, there are no energy storage terms or advection terms. The daytime energy balance is illustrated in figure 2.1. In this case the surface is heated by the net radiation; the heat fluxes transport heat from the surface towards the atmosphere and the soil. Each term will be discussed separately, including an explanation of the interaction with the surface.

The first term in the energy balance equation is the net radiation, Q. It is the sum of both upward and downward long- and shortwave radiation, as given by

$$Q = L + K = L_{down} - L_{up} + K_{down} - K_{up}, \tag{2.2}$$

where L and K represent the long- and shortwave radiation respectively. K describes the incoming (K_{down}) and reflected (K_{up}) solar radiation, therefore K is positive during the day and zero during the night. L the sum of radiation emitted from the atmosphere (and/or clouds) towards the surface (L_{down}) and radiation emitted from the surface towards the atmosphere (L_{up}). L_{down} depends on the temperature and humidity structure of the atmosphere. In principle, L is always negative, except in the presence of (thick) clouds. The clear sky atmosphere is a poor radiator of L, resulting in a weak L_{down} compared to L_{up}. Clouds are strong radiators of L and for cloudy conditions, L_{down} can be as large as L_{up} when cloud temperature is similar to the surface temperature. Therefore, during nighttime Q is either close to zero (clouded) or negative (clear sky), cooling the surface.

The second term in equation 2.1 is the soil heat flux G, resulting from the temperature difference between the surface and deeper soil layers. During the day, the ground surface is heated by solar radiation. Part of that heat is transferred to deeper and cooler soil layers, storing energy in the soil and cooling the surface. This changes during the night when the surface cools rapidly, but deeper soil layers are still warm. Energy is now transported from deeper layers to the surface, warming the surface.

The sensible heat flux H, represents heat that is directly transferred from the earth to the atmosphere, or vice versa, mainly through turbulent transport. The general effect of H on the surface energy balance is shown in figure 2.2, during both daytime (a) and nighttime (b). The daytime temperature decreases with height and turbulent mixing transports warm air from the surface upwards and cool air downwards: H is cooling the surface. The opposite happens during the night when the temperature increases with height, because the surface cools faster than the atmosphere. Now, turbulent mixing transports cool air from the surface upwards and warmer air is transported towards the surface: H is heating the surface. Observations of heating by turbulent mixing, i.e. an increase in H, will be discussed in section 3.4.

The latent heat, $L_v E$, represents the heat transfer from phase changes of water. This term extracts energy from the surface during the day, due to evapotranspiration. As with the other terms, the opposite generally happens during the night, where dew formation and freezing adds energy to the surface.

Strong radiative cooling is found during clear sky nights. This is generally balanced by either H or G. When the night is continuously turbulent, the radiative cooling is balanced by H and the near-surface temperature

remains fairly constant during the night. The temperature difference between the surface and the deeper soil is small, resulting in a small G. If turbulence is weak, i.e. small H, the surface will cool rapidly until a new balance is reached, usually after 2-6 hours [*Van Hooijdonk et al. 2015*]. The surface cools faster than the deeper soil, resulting in a large G. In general, the surface energy balance and the state of the SBL depends mainly on the presence, or absence, of turbulence.

2.2. Turbulence

The intensity of turbulent mixing largely determines the magnitude of H. Turbulent flows have been the subject of scientific research since the end of the nineteenth century. It is an extremely complex process that is still not fully understood. This section only gives a brief introduction, as to facilitate the interpretation of the results in chapters 4 and 5. A more thorough treatment on this topic can be found e.g. in *Nieuwstadt et al. 1998, Tennekes and Lumley 1972*. A few characteristics of turbulence are summarized here following *Tennekes and Lumley 1972*:

- Turbulence is chaotic, or stochastic, in nature. As a result, a deterministic description is not possible, but it can be described statistically.

- Diffusivity of turbulence causes rapid mixing and an increased rate of momentum, heat and mass transport.

- Turbulence is a dissipative process. It requires an energy supply, or it will cease due to internal friction which increases the internal energy (heat) at the expense of turbulence kinetic energy (TKE).

- Turbulence is essentially rotational and three-dimensional, which is a distinction to other chaotic flows (like, e.g., cyclones).

The first step in describing the statistics of turbulence is the Reynolds decomposition [*Reynolds 1895*]. This method splits a signal in a mean signal ($\overline{X}$) and in a fluctuation signal (X'), as is given by

$$X = \overline{X} + X'. \tag{2.3}$$

The mean value generally is an ensemble- or time-related mean, i.e. the mean of an experiment that is repeated an infinite number of times or the mean over a certain time period. When it is subtracted from the original signal, the fluctuating signal X' represents turbulence in many cases, e.g. for wind measurements.

The intensity of turbulence can be characterized by the TKE, often denoted by $\overline{e}$. Since turbulence is a three dimensional process, velocities in three dimensions are considered. Therefore, the velocity vector is decomposed in three components: one vertical velocity (w) and two horizontal velocities (u and v). The definition of kinetic energy in three dimensions is based on wind speed fluctuations and given by

$$\overline{e} = \frac{1}{2}(\overline{u'u'} + \overline{v'v'} + \overline{w'w'}). \tag{2.4}$$

As a dissipative phenomenon, turbulence loses TKE with time and needs a source of energy in order to be sustained. For this study, it is important to understand the processes that generate and suppress turbulence.

The sources and losses of TKE can be found when analysing the two-dimensional budget equation of TKE, given by [*Moene and Van Dam 2014*]

$$\underbrace{\frac{\partial \overline{e}}{\partial t}}_{\substack{\text{term I} \\ \text{time change}}} = \underbrace{-\overline{u'w'}\frac{\partial \overline{u}}{\partial y}}_{\substack{\text{term II} \\ \text{shear production}}} + \underbrace{\frac{g}{\theta_v}\overline{w'\theta_v'}}_{\substack{\text{term III} \\ \text{buoyancy}}} - \frac{\partial \overline{u'e}}{\partial z} - \frac{1}{\rho}\frac{\partial \overline{u'p'}}{\partial z} - \underbrace{\epsilon}_{\substack{\text{term IV} \\ \text{dissipation}}}, \tag{2.5}$$

where u and w are horizontal and vertical velocities, g the gravitational constant, ρ the density, y and z the horizontal and vertical distance, p is the pressure and θ_v the virtual potential temperature. This θ_v represents the theoretical temperature of dry air that would have the same density as moist air, if that parcel was brought adiabatically and reversibly from its initial state to a standard pressure. The equation can be derived from the equations that describe the motion of a viscous fluid in a situation with density stratification for a horizontally homogeneous situation [*Wyngaard 2010*]. To understand the principles behind the sources and losses of TKE, four terms of equation 2.5 are highlighted. The other two terms consider the redistribution of the TKE in space and will not be discussed. The four terms represent the following processes [*Moene and Van Dam 2014*]:

I The change in time of the TKE. When the sum of the right hand side terms is positive, turbulence is generated. When it is negative, turbulence is suppressed and can eventually die out.

II The production of TKE by wind shear. This term can be assumed to be positive, because the average horizontal wind speed generally increases with height and the vertical momentum transport $\overline{u'w'}$ is generally negative near the surface. The magnitude of this term depends on the mean vertical velocity gradient. This production of TKE is at the expense of the mean kinetic energy of the flow.

III Buoyancy describes density fluctuations in a gravity field. This can result in either turbulence generation (positive term) or suppression (negative term), depending on the sign of the virtual heat flux $\overline{w'\theta'_v}$. This will be discussed in more detail in section 2.3.

IV This term describes the loss of TKE to heat due to molecular friction on the smallest scales and always suppresses turbulence.

It becomes clear from equation 2.5 that the buoyancy term (term III) is an important factor in whether or not turbulence is generated ($\frac{\partial e}{\partial t} \geqslant 0$) or suppressed ($\frac{\partial e}{\partial t} < 0$). It is generally the relation between the buoyancy (term III) and the shear production (term II) that determines if turbulence will be sustained or not.

2.3. The concept of buoyancy

Buoyancy in the ABL results from virtual temperature fluctuations θ'_v, which is the virtual temperature difference between a parcel and its surroundings. The principle of buoyancy can be explained through the relation

$$a_{net} = g\frac{\theta'_v}{\theta_v},\qquad(2.6)$$

where, a_{net} can be seen as the effective gravity. This can be derived from the link between temperature and density fluctuation as well as the gravitational and Archimedes force acting on an air parcel [*Moene and Van Dam 2014*]. A warmer parcel, i.e. positive θ'_v, consequently experiences a positive effective gravity a_{net}. The warm parcel experiences positive buoyancy and moves upwards. For parcels colder than their surroundings, i.e. negative θ'_v, the parcel experiences a negative a_{net} and it will move downwards.

It is easy to see how positive buoyancy can enhance turbulence as was mentioned in the previous section. This generally happens during the day when solar radiation heats the surface. Warmer air from the surface moves up due to positive buoyancy, so there is a positive virtual heat flux $\overline{w'\theta'_v}$ in equation 2.5, resulting in turbulence generation.

During the night, the opposite usually happens. In general, the surface cools faster than the atmosphere and the air close to the surface will cool with it. Turbulent mixing will transport cooler air from the surface upwards and warmer air downwards. This will lead to a negative virtual heat flux $\overline{w'\theta'_v}$ in equation 2.5. Therefore turbulent mixing requires energy during the night and turbulence is suppressed by the effect of buoyancy. Using equation 2.5, when negative buoyancy (term III), together with the dissipation of TKE (term IV), is stronger than the shear production (term II), turbulence becomes weaker and can die out. This will lead to stronger stratification of the ABL.

2.4. Boundary layer stability

The most important factors in the stability of the SBL are turbulence and buoyancy, discussed in the previous sections. This section discusses the different regimes of the SBL, which were introduced in chapter 1, based on these two parameters.

There are multiple dimensionless parameters that can give information on the intensity of the TKE. This study will be limited to the interpretation of the (flux-) Richardson number, shown in equation 2.7

$$Ri_f = -\frac{\text{buoyancy production}}{\text{shear production}} = \frac{\frac{g}{\theta_v}\overline{w'\theta'_v}}{\overline{u'w'}\frac{\partial \overline{u}}{\partial z}}\qquad(2.7)$$

The dimensionless Richardson number describes the ratio of the buoyancy production term and the shear production term from equation 2.5. The sign of this ratio gives information of the stability of the ABL, as a number of situations can be distinguished from the Richardson number [*Moene and Van Dam 2014*]:

1. $Ri_f < 0$: There is production of TKE by both buoyancy and shear. These conditions are called unstable conditions.

2. $Ri_f \approx 0$: There is no production or destruction of TKE by buoyancy, but only shear production. These conditions are rare in the ABL and are called neutral conditions.

3. $Ri_f > 0$: There is still production of TKE by shear, but also destruction by buoyancy. These conditions are called stable conditions.

Apart from the sign, the magnitude of Ri_f indicates which of the two terms is dominating. A large Ri_f indicates a dominant buoyancy term. This means that, in an unstable ABL, the rise of warm air is the main generator of turbulence and the height of the ABL will increase significantly. In a stable ABL, it means that the height of the ABL will decrease and that turbulence cannot be sustained in a stationary sense. If the absolute magnitude of the Richardson number is small, shear production dominates and turbulence will be sustained.

As mentioned earlier, the buoyancy term of equation 2.5 is negative during nighttime, resulting is a SBL according to Ri_f. In literature, the SBL is often classified further in the WSBL and the VSBL, which are introduced in chapter 1. A typical representation of the temperature in these regimes is shown in figure 2.3.

The WSBL is found when the shear production of TKE is larger than the suppression by buoyancy. Since shear production dominates in this SBL regime, Ri_f is small. The regime is continuously turbulent and the SBL is relatively well mixed, as shown in figure 2.3a. It is characterized by relatively strong winds, a small temperature inversion (the vertical temperature difference), a small temperature decrease during the night and steady state is quickly reached (within 2-3 h) [*Van Hooijdonk et al. 2015*]. This regime is found during windy and/or cloudy nights, where the surface is heated by turbulent heat transport and/or longwave radiation from clouds, resulting in weak radiative cooling of the surface.

The VSBL is found when buoyancy dominates the TKE budget equation (equation 2.5) and suppresses turbulence, resulting in little mixing, as shown in figure 2.3. Ri_f is large in this regime. It is characterized by weak near-surface winds, a large temperature inversion and a large temperature difference between day and night. Very stable nights reach a steady state after a long transition period (2-6 h) [*Van Hooijdonk et al. 2015*], once a balance between Q and G is reached. This regime is mostly found in clear sky conditions early in the night.

Nights with short-lived turbulent events are found in the VSBL regime, close to the border with the WSBL where turbulence is continuous. Some studies discern a third regime [*Van de Wiel et al. 2003*], the intermittent regime, where the difference between purely radiative nights and nights with intermittent turbulence is acknowledged. This answers the first part of the first research sub-question (RsQ 1) on the meteorological conditions in which short-loved turbulence is found. The definitions of these regimes in literature do provide useful information to identify nights with short-lived turbulence, as is discussed in section 3.3.
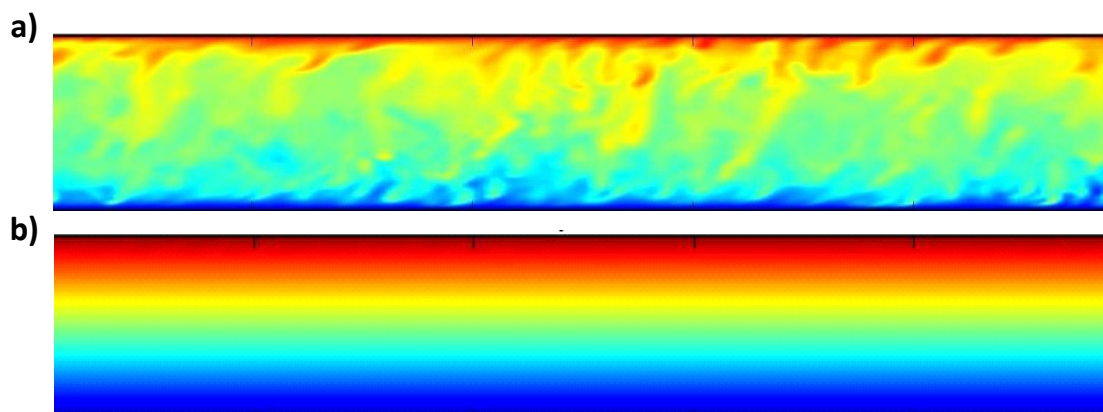

Figure 2.3: An illustration of the temperature distribution with height for the WSBL (a) and the VSBL (b), where red and blue indicate warm and cold air respectively. The WSBL is characterized by strong winds, resulting in dominant production of turbulence by wind shear and strong turbulent mixing. The temperature in this regime is relatively uniform. The VSBL is characterized by weak winds and is dominated by turbulence suppression by buoyancy. Turbulent mixing is weak, resulting in strong stratification. [*Donda 2015*]

3

Methodology

After discussing the theoretical background on turbulence and boundary layer stability, the methodology used to study the turbulent structures is described in this chapter. The first section describes the observational networks, in particular the spatial configuration of the micro-meteorological stations. Section two describes the parameters used in this study, and the instruments to observe them. The third section describes the selection process to find nights with short-lived turbulence. Section four discusses the expected correlation between fluctuations in wind speed and near-surface temperature for short-lived turbulence. This leads up to the final section, which describes the methods to study the spatial scale of the short-lived turbulent structures. It describes two methods: a visual analysis method and the station correlation analysis method.

3.1. Observational networks

The Cesar Observatory, often referred to as the Cabauw Tower or simply Cabauw, is located in the western part of the Netherlands in a polder 0.7 m below sea level. The large number of instruments at the site are used to study the atmosphere and its interactions with the surface. The main feature of the site is the 213 m high tower, holding many instruments at different heights. Observations of many instruments at Cabauw are first used in this study to gain understanding of short-lived turbulent events. Observations from Cabauw are also used to select cases with short-lived turbulence (section 3.3) and to validate the use of wind speed and near-surface temperature observations to observe turbulence (section 3.4). Finally, the observations are used to develop methods to study the spatial scale of the turbulent structures (section 3.5).

The KNMI owns and maintains a network of automated weather stations (AWS) in the Netherlands. This study uses temperature observations from these stations at 2 m and 0.1 m, as well as the wind speed and direction at 10 m. Observations from 32 stations on land observe both temperature and wind speed and are used in this study. These stations observe several additional parameters, as is shown in figure 3.1. Some also observe cloud cover, not shown in this figure. The location of each station, as well as the availability of cloud cover observations, are shown in figure 3.2, where Cabauw is highlighted with the letter C. The average distance between neighbouring stations is 32.5 km. In text, stations are referred to by the letters AWS, followed by the station index, e.g. Cabauw is referenced as AWS348. The AWS network is used as the first step in studying the spatial scale of short-lived turbulent structures and the results are discussed in chapter 4.

Schiphol Airport is located 9 km southwest of Amsterdam at an elevation of 3 m below sea level. Its main observational station is part of the KNMI AWS network. There are two identical AWS fields and 6 wind poles at the airport. In addition, there are 4 visibility stations around the airport, which also measure temperature and wind speed. The complete network used in this study is shown in figure 3.3, consisting of observations at the airport (red), the 4 visibility stations (blue) and the KNMI AWS within a radius of 40 km from the airport (black). The average distance between neighbouring stations is 8.2 km, with an average distance of 1.9 km for neighbouring stations in the core of the network. The network is also maintained by the KNMI and the same standards apply. For simplicity the stations are referred to in text as AWS, followed by the station index, similar to the AWS network. It is the second network that is analyzed and the results are discussed in chapter 5. Note that at Schiphol Airport, most stations are close to one of the runways. A more detailed description of the network, including the indexing of the stations, can be found in Appendix A.
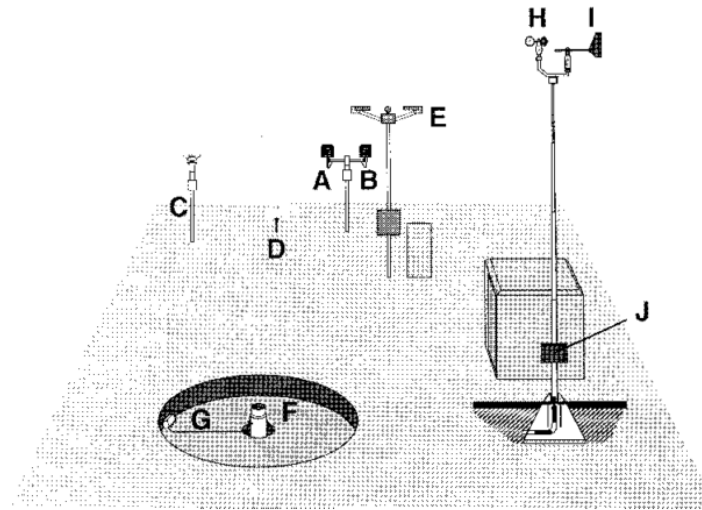
A	temperature (°C)	F	precipitation (mm)
B	humidity (%)	G	precipitation period (min)
C	global radiation (Joule/cm^2)	H	wind speed (m/s)
D	gras minimum temperature (°C)	I	wind direction (degree)
E	visibility	J	air pressure (hPa)

Figure 3.1: A diagram of an automatic weather station from the KNMI Handbook for the Meteorological Observation, using AWS 367 Stavoren as an example. This figure shows the instrument set-up and the parameters that are measured at a standard AWS.
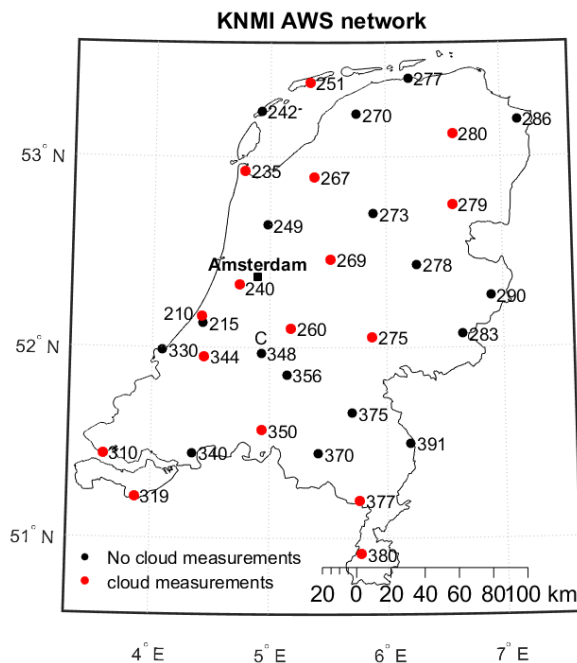

Figure 3.2: The location of the 32 AWS of the KNMI network in the Netherlands. The number near the location is the station index. A black station does not measure the cloud cover, while a red station does. The station with index 348 and highlighted with a 'C' over it is the Cabauw site.
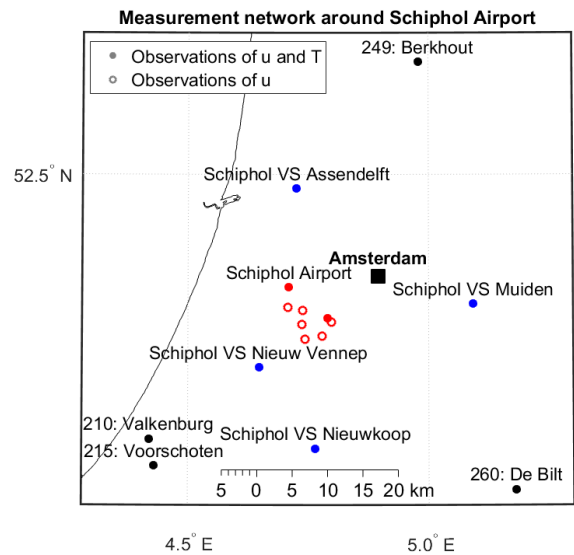

Figure 3.3: The Schiphol Airport network is made up of three sections: observations at the airport (red), visibility stations (blue) at 10 to 20 km from the airport and KNMI AWS (black) about 40 km from the airport. The stations shown as an empty circle only measure the wind speed, while the other stations also measure the temperature at 0.1 and 2 m.

3.2. Instruments

This section describes the instruments from which the measurements used in this study were obtained. Each parameter, as well as the instruments to observe it, will be discussed separately.

3.2.1. Temperature

The air temperature (T) is measured at 0.1 m ($T_{0.1m}$) and 2 m T_{2m} at all KNMI stations and in addition at 10, 20, 40, 80, 140 and 200 m at Cabauw. A platinum resistor element, the KNMI Pt500-element, is used in an unventilated KNMI temperature hut. Temperature is measured with an accuracy of 0.1^oC. The 0.1 m sensor is positioned in a special radiation protector. The surface is covered with short grass at all KNMI sites, with a length of 3 cm or less. Both 10 minute and 1 minute data are used for the KNMI AWS and the Schiphol Airport network. The 10 minute data of the 0.1 m temperature is the minimum temperature measured during the 10 minute interval. At other heights, this data is the 10 minute average.

3.2.2. Wind

Wind speed (u) is measured as the horizontal wind speed of air in meters per second (ms^{-1}), using a cup anemometer. It registers the average value of the wind speed over the last three seconds, every quarter of a second. It is measured at the KNMI AWS at a height of 10 m u_{10m} and in addition at 20, 40, 80, 140 and 200 m at Cabauw. Wind speed is measured with an accuracy of $0.5ms^{-1}$ when $u \leqslant 5ms^{-1}$ and ±10% when $u > 5ms^{-1}$.

Wind direction (u_d) is measured every 12 seconds in degrees (degrees of arc). The direction represents the meteorological wind direction, where 0° and 90° represent the north and east respectively. It is measured at the same heights as the wind speed, using a weather vane. The measurement resolution is 1° with an accuracy of ±3 degrees for $u \geqslant 2ms^{-1}$.

Note that both speed and direction are preferably measured at a height of 10 m. While most stations do measure at 10 m, some measure at the minimum height of 6 m, e.g. at Voorschoten (AWS215). This can have an effect on the measurements, since it is expected that the wind speed increases with height. Both 10 minute and 1 minute data are available for the AWS network and the Schiphol Airport network.

3.2.3. Clouds

Cloud cover is measured using a lidar (LIght Detection And Ranging) system: the Vaisala LD-40 ceilometer. It measures the cloud cover of the sky dome in octants, where 0 indicates clear sky and 1 to 8 indicate the fraction of the sky dome is covered. The number 9 indicates that the sky cannot be detected, for example due to fog.

At Cabauw, the cloud cover is measured using the NubiScope instrument. It measures the sky temperature in the thermal infra-red and returns the cloud cover in percentages for the sky dome. It scans every 10 minutes and measures the sky temperature at 36 azimuth and 30 zenith angles. From the NubiScope measurements, the obstruction type can be determined, for example broken clouds or light fog.

3.2.4. Radiation

Three types of radiation measurements at Cabauw are used in this study: L_{down}, K_{down} and Q. The L_{down} is measured at Cabauw using the Kipp & Zn CG4 pyrgeometers, mounted at a height of 1.5 m. This parameter is used to determine the effect of clouds, as was discussed in section 2.1. These observations are used for the case selection procedure and will be discussed in section 3.2.

The K_{down} is measured at Cabauw using the Kipp & Zn CM22 pyranometers and are mounted at a height of 1.5 m and at the same location as the L_{down} instruments. K_{down} is zero during the night and is used to determine the time of sunset and sunrise.

Q is measured at Cabauw using a Schulze net radiometer type LXG055 (Schulze-Daeke type) and is positioned at a height of 1.5 m. The instrument measures the total, long and short wave, downward radiation and the total upward radiation separately. The Q is derived from these measurements following equation 2.2. In this study, radiation measurements are used during the case selection (section 3.2), as to filter cases with substantial cloud coverage.

3.2.5. Turbulence parameters

Two turbulence parameters were used for the case selection: the friction velocity (u_*), and the sensible heat flux (H), which was discussed in section 2.1. Both parameters are observed at Cabauw. H is derived by

means of eddy correlation technique, using fluctuations due to turbulence of wind speed, temperature, humidity and CO_2. These parameters are measured using a combination of two instruments: A sonic anemometer/thermometer, measuring the wind vector and sonical temperature, and an optical open path sensor (H_2O and CO_2). From H and the 10 m wind speed, u_* is derived and expressed in ms^{-1}.

3.2.6. Additional data

In addition to the ground-based observations at Cabauw and the AWS, other sources of information were used during the case selection of section 3.3. To make sure that the observed features are more a result of 'internal dynamics' rather than a direct consequence of changing external forcings, synpotic weather maps are studied. These maps are available every 6 hours[1] and an example is shown in figure 3.4, which shows the conditions over Europe on 0:00 UTC on the 15th of April 2015. The symbols that are found in these weather maps are explained in table 3.1.

In addition to the cloud cover observations, satellite images are used to see if the nocturnal sky is clear. Infrared images from the SEVIRI instrument on the METEOSAT geostationary satellite are used to create these images. These images are available every three hours[2]. By using infrared channels, clouds can be detected during both day and night. An example can be found in figure 3.5, showing the cloud cover over Europe at the same time as figure 3.4.

3.2.7. Data availability

This study uses data from August 2013 up to and including April 2016, because of the availability of the data. Both the KNMI AWS and Cabauw have long records of their observational data, but it was not until August 2013 that $T_{0.1m}$ observations were added to the observational site at Cabauw. Cloud observations of the NubiScope instrument at Cabauw were only available up to and including April 2016. In total, 1004 nights are studied.

For the observed parameters at Cabauw and at the AWS network, a temporal resolution of 10 minutes is studied. The spatial resolution of the Schiphol Airport network is much higher. This network is studied in more detail with a temporal resolution of 1 minute for the u_{10m} and $T_{0.1m}$ observations.

---

[1] https://www.knmi.nl/nederland-nu/klimatologie/daggegevens/weerkaarten
[2] http://www.woksat.info/wos.html

Table 3.1: A description of the symbols used in Dutch synoptic weather maps.

Symbol	Description
	Red halve circles on a red line display a warm front. It is often accompanied by long lasting rain, increasing cloud cover and/or slow temperature increase.
	A cold front is displayed by blue triangles on a blue line. It is often accompanied by a temperature decrease and unstable weather with a high occurrence of heavy showers and thunder storms.
	An occluded front is displayed by purple triangles and half circles on a purple line. It forms when fast moving cold front meets a slow moving warm front. It is usually accompanied by unstable weather with a lot of rain.
	A stationary front is displayed by both red half circles and blue triangles. It is often located between two high pressure systems and hardly moves as a result. The weather is often characterized by a thick cloud layer, some small precipitation and low winds.
	A trough is displayed as a thick blue line. It is a region with relatively low pressure and is connected to a low pressure area where the isobars are closest, which is often behind a cold front. It is often accompanied with rainy weather.
	A ridge is displayed by a thick red line. It is a elongated area of high pressure and a spur of a high pressure area. It is often accompanied by stable weather.
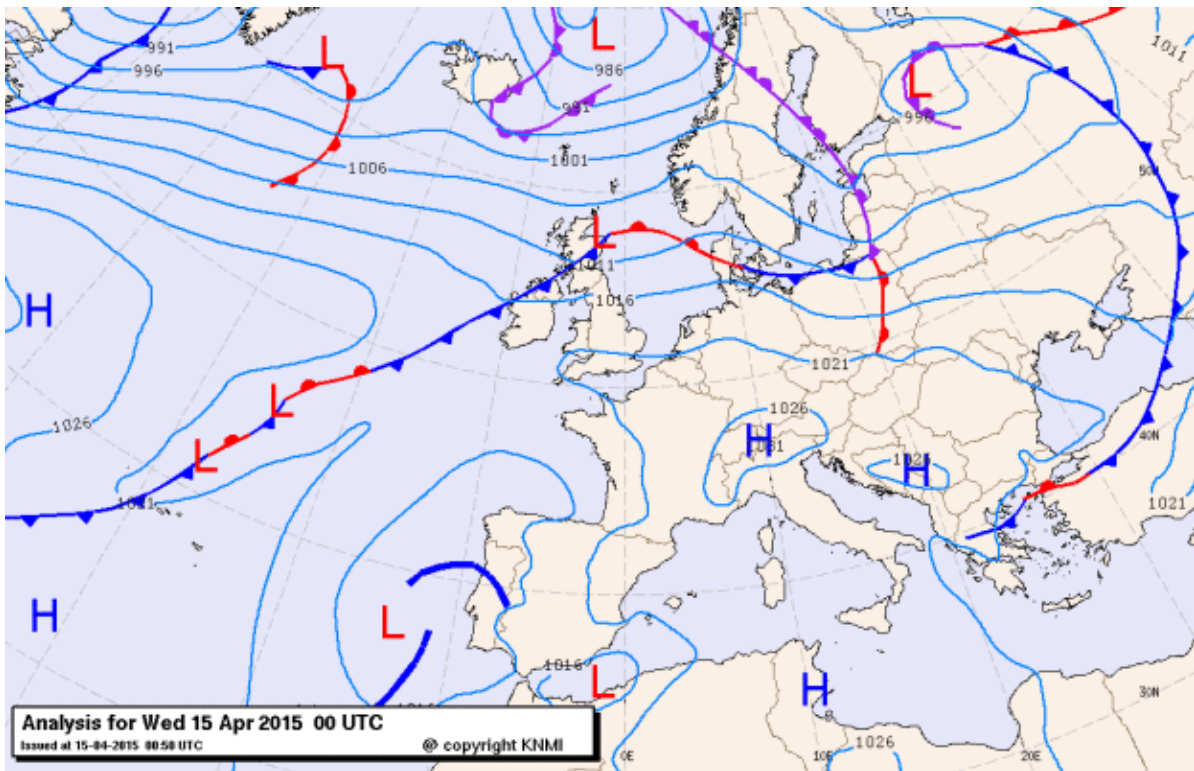
Figure 3.4: The synoptic weather map of case 3: the night of the 14th to the 15th of April 2015. This figure shows a stable high pressure area over the mainland of Europe and presence of a low pressure system over Scotland.

Figure 3.5: The cloud cover over western Europe from infra-red measurements of the SEVIRI instrument of the METEOSAT satellite. The image is taken on the 15th of April 2015 at 0:00 UTC. The sky over the Netherlands is predominantly clear at this time, except for the far northeast of the country.

3.3. Case selection
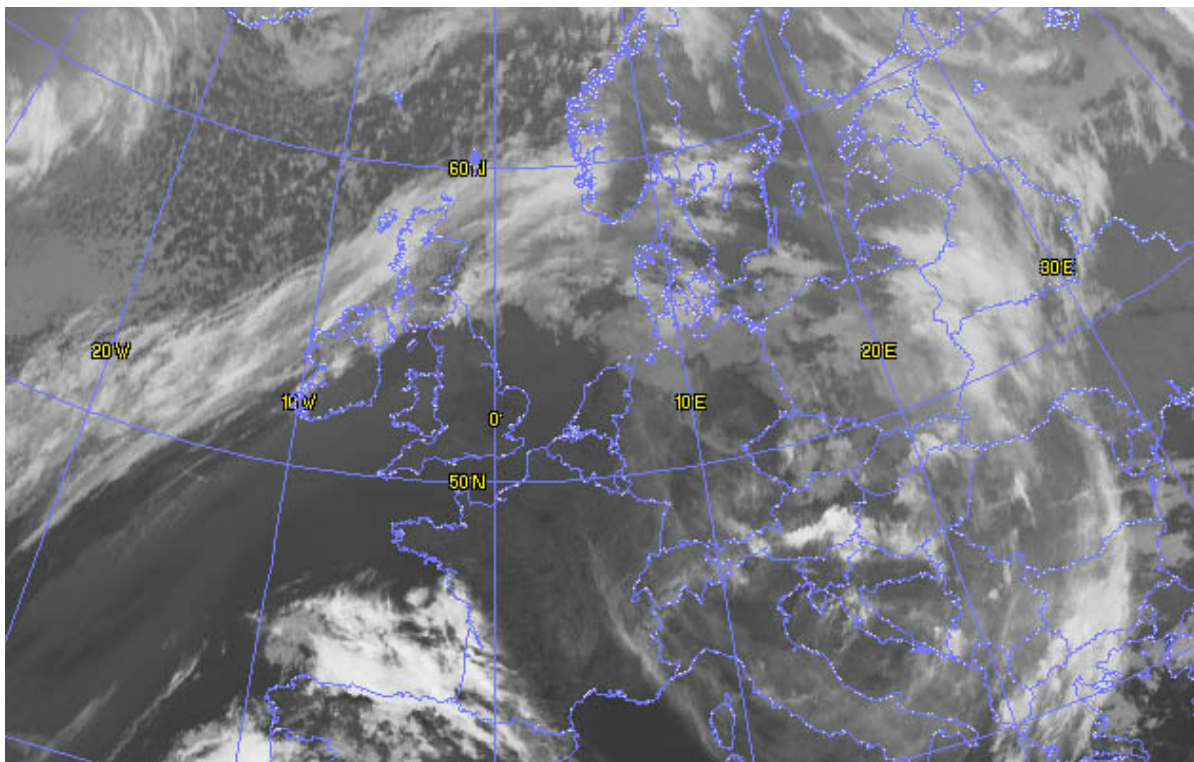
A first selection of nights with short-lived turbulence is made using an automated selection procedure. The selection is made using observations from Cabauw. As was discussed in section 2.4, it is expected that nights with short-lived turbulence are found in the VSBL regime, as well as the intermittent regime. In this section, the theoretical knowledge from chapter 2 will be translated to observable criteria to find cases of short-lived turbulence, thus answering the second part of the first research sub-question (RsQ 1). The criteria of the automated selection filter are based on the following characteristics of these two regimes:

- Weak and intermittent turbulence

- A clear sky

- A large temperature inversion

- A large temperature decrease from day to night time

At night, turbulence is generated by wind shear, as shown by equation 2.5. As such, it is assumed that the strength of turbulence will be related to the magnitude of the wind near the surface. Here, the wind at 40 m height (u_{40m}) is uses as an indicator of the mechanical forcing of the boundary layer at night. During the evening, winds weaken near the surface [*Lapworth 2008*] while accelerating at higher levels [*Blackader 1957*]. At the crossing height, estimated to be close to 40 m at Cabauw [*Van de Wiel et al. 2012*], u remains relatively constant over the course of the diurnal cycle. As it is less affected by local stability effect than e.g. the 10 m wind, u_{40m} can also seen as a proxy for the large scale wind forcing. The large scale wind forcing needed to sustain steady near-surface turbulence under clear sky conditions, is estimated to be $5 - 7$ ms^{-1} according to *Van de Wiel et al. 2012*. As a criterion, the average u_{40m} is not allowed to exceed 7 ms^{-1} during the night.

Turbulence can be triggered by variations in the cloud cover as a result of their radiative properties and strict critaria are required to filter out clouded nights. Traditional clear sky criteria using Q, e.g. used by *Van Hooijdonk et al. [2015]*, are not sufficient. A new set of criteria is made based on the cloud cover percentage
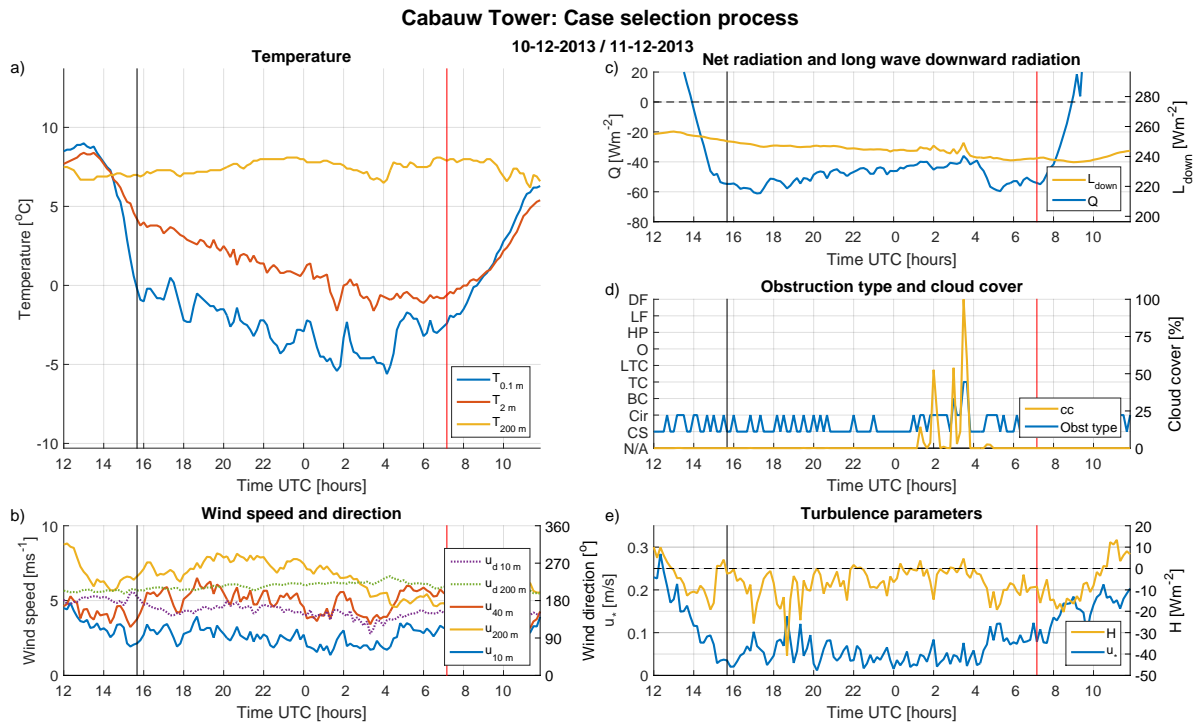
Figure 3.6: The manual selection process uses a single figure that shows observations from Cabauw of temperature (a), wind speed and direction (b), radiation (c), cloud cover (d) and turbulent parameters (e). The observations are shown for a time period of 24 hours, starting at 12:00 UTC, where sunset and sunrise are indicated by black and red vertical lines respectively. This example shows a night with clear fluctuations in both $T_{0.1m}$ (a), u_{10m} (b) and the turbulent heat flux and the turbulent friction velocity (e). Between 2:00 and 4:00 UTC, some clouds are observed (d), but their radiative effect is relatively small based on the radiative measurements (c).

and the L_{down}. Nights with a mean cloud cover larger than 30% are discarded. In addition, a L_{down} boundary value is set at the nighttime minimum L_{down} plus $30 Wm^{-2}$. Nights where more than 25% of the nighttime measurements exceed this boundary are discarded. This criterion removes significantly clouded nights, while allowing edge cases, for example clear nights ending in fog, to pass through.

The physical characteristics of the nocturnal regime are strongly reflected in the near-surface temperature signal. For example, a strong inversion and a large day to night difference in $T_{0.1m}$ is only found when turbulence is weak. Therefore, temperature observations at different heights are useful to detect whether a VSBL is present. As a first T criterion, the temperature difference between 200 m and 2 m has to be at least 3^oC at one point during the night. As a second T criterion, the amplitude of the diurnal T_{2m} signal, i.e. the difference between maximum daytime and minimum night-time temperature, has to be at least 6^oC.

The final automated criterion discards nights in which more than 10% of the T and u data is missing. When applying these criteria to the nights from August 2013 up and including April 2016, the dataset is reduced to a subset of 146 nights (15%). The automated filter is not sufficiently accurate to only capture nights with short-lived turbulence; some continuous turbulent nights and purely radiative nights are included as well. A second selection, done manually, is applied to this subset. The remaining cases will be used to study short-lived turbulent events.

The manual selection is done by individual inspection of all nights in the subset using 5 panel figures, such as figure 3.6. It shows observations of T at different heights (3.6a), u and u_d at different heights (3.6b), Q and L_{down} (3.6c), cloud cover (3.6d), and both H and u_* (3.6e). The black and red vertical lines indicate the time of sunset and sunrise respectively. The case selection aims to find nights with clear and concurrent increases in both u_{10m} and $T_{0.1m}$, as well as perturbations in the other parameters. The synoptic weather map and the SEVERI infra-red images are considered during the manual selection. Clouded events are excluded by discarding nights where the perturbations in Q and L_{down} have similar characteristics.

Manual selection reduces the number nights from 146 nights (15%) to a subset of 44 nights, 4% of the original dataset. This subset contains nights with clear short-lived turbulent events, or edge cases with very weak turbulence. Even though the conditions seem good, clear short-lived turbulent events are not found at Cabauw in the latter cases. These cases are included because clear short-lived turbulent events could be found at other locations. The small subset of nights resulting from the manual selection confirms the expectation that the conditions for short-lived turbulence are not often found in the Netherlands. Therefore, the present study focuses on an in-depth analysis of a few particular events. In answer to research sub-question 1 (RsQ 1); it is the combination of automated criteria and visual criteria, based on characteristics of the VSBL, that are required to select cases of short-lived turbulence.

These particular events are selected from the subset of 44 nights by a second manual selection process. This final selection only retains the clearest examples of short-lived turbulence over a range of lengths and intensities. The final selection for the AWS network is based on observations of Cabauw and consist of 7 nights, shown in the first column of table 3.2. The conditions at Schiphol Airport, 42 km north-northwest of Cabauw, can be different from Cabauw. Therefore, a new selection is made for the Schiphol Airport network, consisting of 11 nights, shown in the second column of 3.2. All results of this study are based on observations from these analysis subsets.

Table 3.2: The date of the nights in the analysis subsets for the AWS network (column 1) and the Schiphol Airport network (column 2).

Final selection AWS network	Final selection Schiphol Airport network
10-12-2013 to 11-12-2013	10-12-2013 to 11-12-2013
11-09-2014 to 12-09-2014	03-07-2014 to 04-07-2014
15-02-2015 to 16-02-2015	17-03-2015 to 18-03-2015
14-04-2015 to 15-04-2013	23-03-2015 to 24-03-2013
17-04-2015 to 18-04-2005	14-04-2015 to 15-04-2005
01-10-2015 to 02-10-2015	19-04-2015 to 20-04-2015
16-02-2016 to 17-02-2016	06-08-2015 to 07-08-2015
	31-10-2015 to 01-11-2015
	17-01-2016 to 18-01-2016
	16-02-2016 to 17-02-2016
	12-04-2016 to 13-04-2016

3.4. Correlation between wind speed and near-surface temperature

An extensive observational network often requires relatively cheap instruments in order to make it financially viable. In order to get a high spatial resolution, many instruments are needed. A similar principle applies when looking for an existing network where high spatial coverage is important. Relatively cheap instruments are widely used and make up a dense observational network. It is for that reason that wind speed observations and near-surface temperature observations are used in this study. From the previous analysis in chapter 2, it is expected that some correlation between perturbation in wind speed and near-surface temperature could exist. In this section this correlation will be quantified to validate the use of these parameters to study short-lived turbulence.

Short-lived turbulence is characterized by a sudden and short lived increase in wind speed. Due to turbulent mixing, similar fluctuations are found in the near-surface temperature. These turbulent fluctuations can be extracted from the observations by subtracting a moving average from the $T_{0.1m}$ and u_{10m} observations. In this study, a weightless moving average with a window of 190 minutes is used. The resulting fluctuations are referred to as moving average temperature fluctuations ($MATF$) and moving average wind fluctuations ($MAWF$). As long as there are no clouds, it is assumed that the fluctuations of the $MATF$ and the $MAWF$ are only the result of turbulence.

A visual analysis, comparing the two moving average fluctuations, is used to see if the two signals are indeed related. This relation is then quantified using the correlation coefficient $R_{X,Y}$ as shown below:

$$R_{X,Y} = \frac{\overline{X'Y'}}{\sigma_X \sigma_Y} \tag{3.1}$$

Where X and Y are the two parameters of which the correlation is calculated. The correlation coefficient ranges from -1 to 1, with perfectly correlated signals having an $R_{X,Y}$ of 1, uncorrelated signals having an $R_{X,Y}$ of 0 and negatively correlated signals having a $R_{X,Y}$ of -1. As a visual aid, a scatter plot of the $MAWF$ against the $MATF$ will be shown together with the $R_{MAWF,MATF}$ value.

In all cases with distinct turbulent events, a clear relation between the two parameters was found with a visual analysis. As an example, turbulent fluctuations from the same night as figure 3.6 are shown in figure 3.7. This figure shows the time series of the $MATF$ (purple) and $MAWF$ (yellow) and the two clearly show a strong coherence. However, the $R_{MAWF,MATF}$ of 0.36 indicates that the correlation is weak, as is also suggested
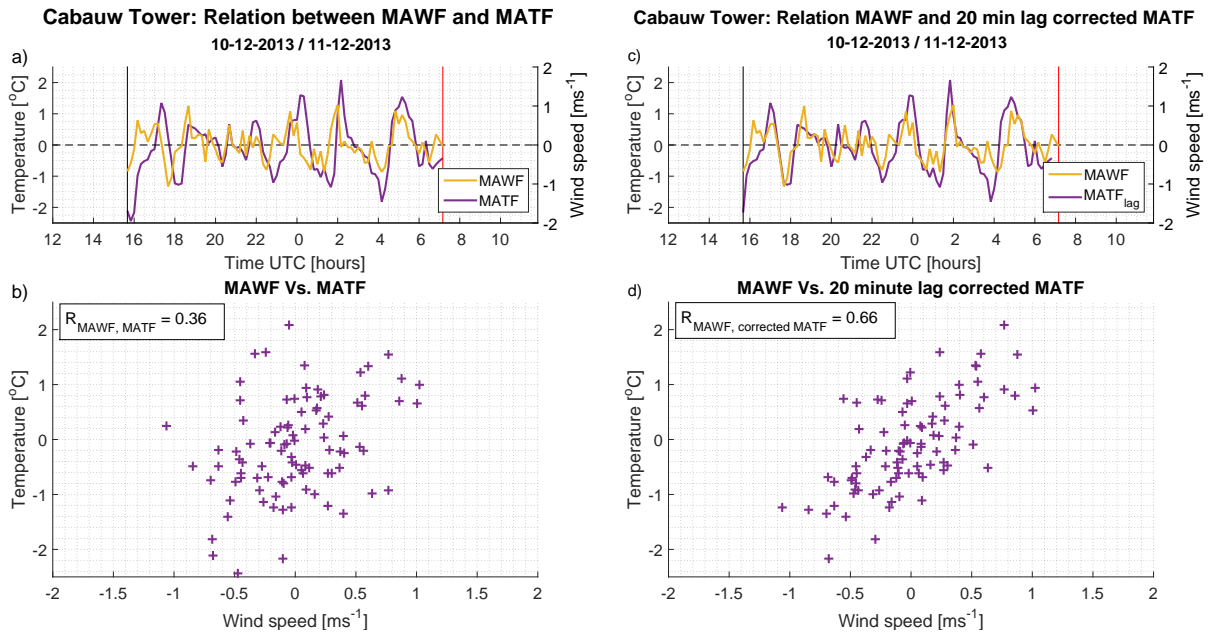

Figure 3.7: Time series of the $MATF$ (purple) and the $MAWF$ (yellow) are shown in a. A scatter diagram of the $MAWF$ against the $MATF$ is shown in b. The relation between the two parameters is quantified by the correlation coefficient $R_{MAWF,MATF}$ in the top left of the image. An $R_{MAWF,MATF}$ of 0.36 indicates a weak relation. The image in c is the same as in a, but now comparing the $MAWF$ with the $MATF$ that is corrected for a 20 minute time delay. Image d is similar to image b, but also compares the $MAWF$ with the lag corrected $MATF$, i.e. $correctedMATF$.

by the large spread in the scatter plot of figure 3.7b.

The most likely reason for the disagreement between the visual analysis and the correlation coefficient is a delayed response of the temperature. The temperature only increases once the wind speed is sufficiently strong to cause turbulent mixing and it only decreases again once the wind speed is not strong enough to sustain turbulence. A second reason for the delay is thermal inertia; the degree of slowness with which the temperature of a body approaches that of its surroundings. The $MATF$ signal can be corrected for this delay, by finding the delay at which the cross-correlation between the two signals is maximum.

When this correction is applied, the overlap between the signals in figure 3.7c has improved compared to figure 3.7a. The $R_{MAWF,correctedMATF}$ increases to 0.66 which is reflected by the stronger linearity of the scatter diagram, as shown in figure 3.7d. The same relation was found using a method that manually extracted the turbulent fluctuations from the observations. This other method turned out to more time intensive and less consistent compared to the method using a moving average. The comparison of the two methods and their results can be found in table B.1 of Appendix B. These results show that the $T_{0.1m}$ and u_{10m} observations are indeed related and can be used to study turbulent events. It also shows that the $MAWF$ is effective in capturing turbulent fluctuations.

By showing that u_{10m} and $T_{0.1m}$ are valid parameters to observe short-lived turbulence, the second research sub-question (RsQ 2) is answered. This is a promising result for the answer to the first research question (RQ 1). Both u_{10m} and $T_{0.1m}$ are measured at (nearly) all stations in the previously described networks (section 3.1), therefore the tools are available to observe the structures. It will depend the scale of the structures, or the station density of the existing networks, if short-lived turbulent structures can be observed or not. This is studied in chapters 4 and 5.

3.5. Network analysis methodology

The analysis of turbulent structures using network observations is done by two methods: a visual analysis and the station correlation analysis. This section describes the analysis process of both methods. Note that the two methods are applied stepwise. First, the visual analysis has to show that there are structures reaching multiple stations. Only then is the second method, the station correlation analysis, applied.

The visual analysis studies time series of $T_{0.1m}$ and u_{10m} observations. Neighbouring stations are visually compared, with the aim to find (near-)simultaneous short-lived turbulent events with similar characteristics. When a turbulent event with similar characteristics is found around the same time at neighbouring stations, it is assumed that these stations observe the same turbulent structure.

Propagation of structures is studied by studying two sets of stations which (more or less) form two straight lines perpendicular to each other, resembling a cross. An example is shown in figure 3.8. In this example, a red and a blue transect, i.e. a line of the cross, are shown. Cabauw is shown in black in figure 3.8 and is the center of the cross. It is used as a reference and is part of both the red and the blue transects. When a turbulent signal is found at multiple stations, the propagation direction can be inferred from the event time lag between the stations. This method is referred to as the "cross method".

When the visual analysis indicates that the size of the turbulent structures is sufficiently large to reach multiple stations, a station correlation analysis is applied. This method is applied to a small time window, called the "analysis window", in order to study a single turbulent event. The station correlation analysis calculates the correlation coefficient (equation 3.1) between the $MAWF$ (within the analysis window) of all station combinations. The $MAWF$ is used, because wind speed is observed at every station and it captures turbulent fluctuations well, as is described in section 3.4. Using both the correlation coefficients and the distances between stations, an estimation can be made of the size of the structure.

When the turbulent signals of two stations are correlated, it is assumed that the size of the turbulent structure is larger than the distance between these stations. Note that the signals become decorrelated for a time delay between the signals. If there is a time delay, it means that the structure moves from one station to the other. Both stations are affected by the structure, which is different from the size of the structure.

It is expected that the correlation coefficient between stations decreases with distance. Therefore, a scatter diagram is made showing the correlation coefficients against station distance. It is assumed that this decrease can be described as an exponential decay, described by:
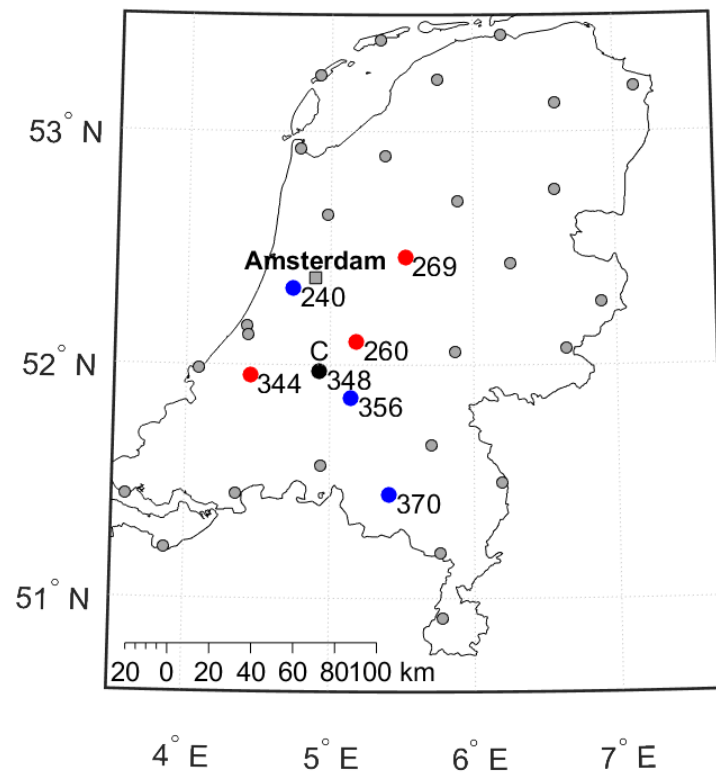
$$y(x) = e^{-x/C}. \tag{3.2}$$

Figure 3.8: An example of two crossing lines, made from stations in the AWS network. Cabauw (AWS348) is shown in black since it is part of both lines. By studying the observations on these two lines, an estimation of the propagation direction of the turbulent structure can be made.

A fit, according to this exponential decay, was made to the data in the scatter diagram. By forcing the fit to start at 1, large residuals are expected at a certain distance, because a large and random spread in the correlation coefficients is expected once the signal becomes de-correlated. In a similar fashion, residuals are also expected at very small distances because of local differences resulting in slight differences in the turbulent signal. It is expected however, that correlation will be significant enough at short distances for this method to be viable.

When using equation 3.2 in the station correlation method, x represents the distance between stations and y represents the correlation coefficients. The only constant C in equation 3.2, is estimated using non-linear least squares. The $MAWF$ signal is assumed to be uncorrelated when the fit reaches the e-folding distance, i.e. the distance at which the fit reaches a correlation coefficient of $1/e$, i.e. 0.368. The e-folding distance is equal to C, as described in Appendix C. Note that using a one-dimensional e-folding distance, spatial isotropy of the structure is assumed.

This leads to the answer of research sub-question 3 (RsQ 3). Visual analysis is required as a filter as to identify that the turbulent structure spans multiple stations. If so, the e-folding distance is used as an estimation of the scale of the turbulent structures, by applying the station correlation to the observational data of the networks.

4

Analysis of the AWS network

The described analysis methods are first applied to the AWS network. All cases form the final selection, the 7 cases shown in table 3.2, are studied. Here, two particularly interesting cases from this subset are discussed. These cases are exemplary for the overall conclusions drawn from the analysis of the AWS network. The first section describes the results of these two cases. A discussion and the conclusions of the general results of the analysis of the AWS network are found in the second section.

4.1. Results

The first case is the night of the 14th to the 15th of April 2015. Observations from Cabauw (AWS348) and the two closest stations, De Bilt (AWS260) and Herwijnen (AWS356), are studied. Figure 4.1 shows the night-time observations of $T_{0.1m}$ (a) and u_{10m} (b) as well as the locations of the stations (c) with colors corresponding to the time series. On this night, two distinct turbulent bursts were observed at Cabauw (shown in black) at 22:30 and 1:30 UTC. These events are not found at AWS260 and AWS356, but they do observe a single turbulent burst at 20:30 and 21:30 UTC respectively.

The observed turbulent signal at Cabauw has very different characteristics than the signals at the other two stations. Cabauw experiences a long period of turbulence between 23:00 and 3:30 UTC, while there is no
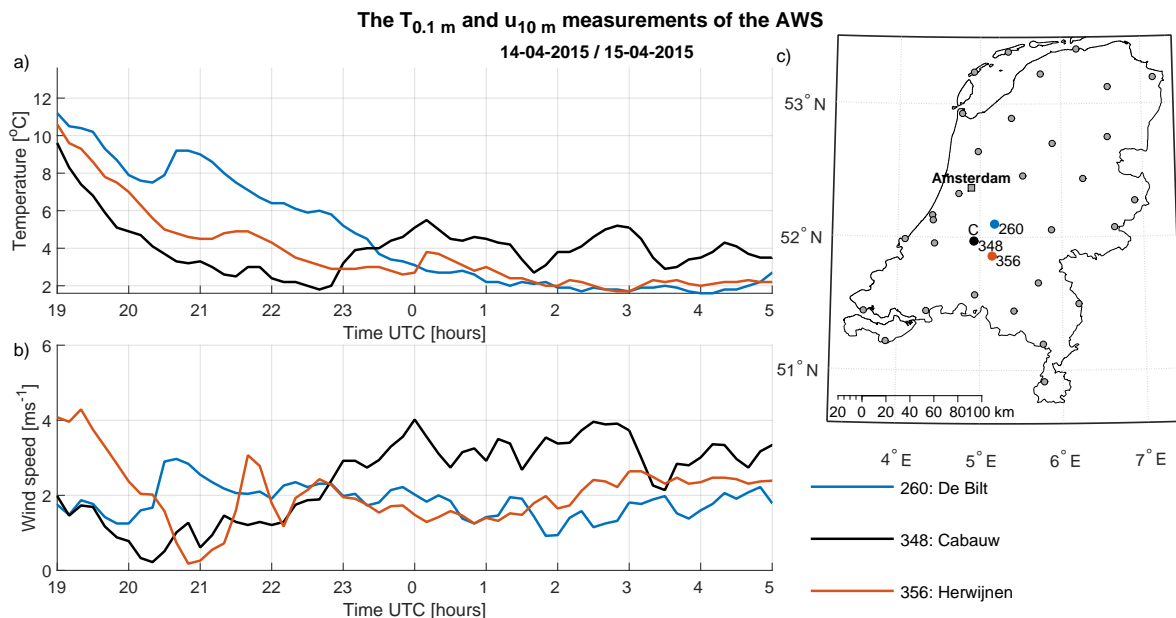

Figure 4.1: The $T_{0.1m}$ (a) and u_{10m} (b) observations on the night of the 14th to 15th of April 2015, as well as the location of the AWS (c). All three stations show at least one distinct turbulent burst, but they do not show similar characteristics in neither $T_{0.1m}$ nor u_{10m}. Both AWS260 and AWS356 do show a single turbulent event at 20:30 and 21:30 UTC respectively.

significant turbulence found at the other two stations. At AWS260 and AWS356 however, a single short burst of turbulence is observed around 20:30 and 21:30 UTC respectively. These turbulent burst do not seem to be related, because of their different characteristics and the long time between the two.

The second case is the night of the 16th to the 17th of February 2016. This case does show a relation between Cabauw and its neighbouring stations. This night is studied by applying the cross method, using the same stations as described in section 3.5 and figure 3.8. Figures 4.2 and 4.3 show the $T_{0.1m}$ (a) and u_{10m} (b) observations, as well as the location of the stations (c), of the first (blue) cross line and second (red) cross line respectively. Cabauw, is part of both cross lines as a reference and is shown in black in both figures.

The two figures show that multiple turbulent events are found at Cabauw. Between 18:00 and 19:30 UTC, a strong turbulent burst causes a large increase in both $T_{0.1m}$ and u_{10m}. Turbulence dies out until 22:00 UTC. At that moment, the wind speed picks up and the near-surface temperature increases. This is a result of the heat transport from turbulent mixing, as is discussed in section 2.1. The two turbulent events have specific characteristics. The first event is characterized by a short and sudden turbulent burst, while the turbulent intensity increases more gradually during the second event. Turbulent events with similar characteristics are looked for in neighbouring stations.

The cross method is used to study the two distinct events. Station observations from the ('vertical') blue transect of the cross method (figure 3.8) are shown in figure 4.2. In this figure, the turbulent burst at 18:00 UTC at Cabauw is only observed at AWS356. At this station, a small u_{10m} increase is observed at 18:15 UTC, followed by a strong decrease at 19:30 UTC. The $T_{0.1m}$ observations show a weak response to u_{10m} changes at this station. The other two stations do not observe significant turbulence between 18:00 and 20:00 UTC.

Around the time of the second event at Cabauw (between 22:00 and 2:00 UTC), turbulent events are found at the other stations as well. The largest event is found at AWS240 between 22:30 and 2:30 UTC. The large u_{10m} increase, from 1 to 5 ms^{-1}, results in a increase in $T_{0.1m}$ of 4^oC. An increase in u_{10m} of nearly 3 ms^{-1} is observed between 23:00 and 2:00 UTC at AWS356, but there is no clear $T_{0.1m}$ response. This station also observes a couple of smaller turbulent events round 22:00 and 3:00 UTC. AWS370 measures turbulence at a later time, between 1:30 and 5:00 UTC.
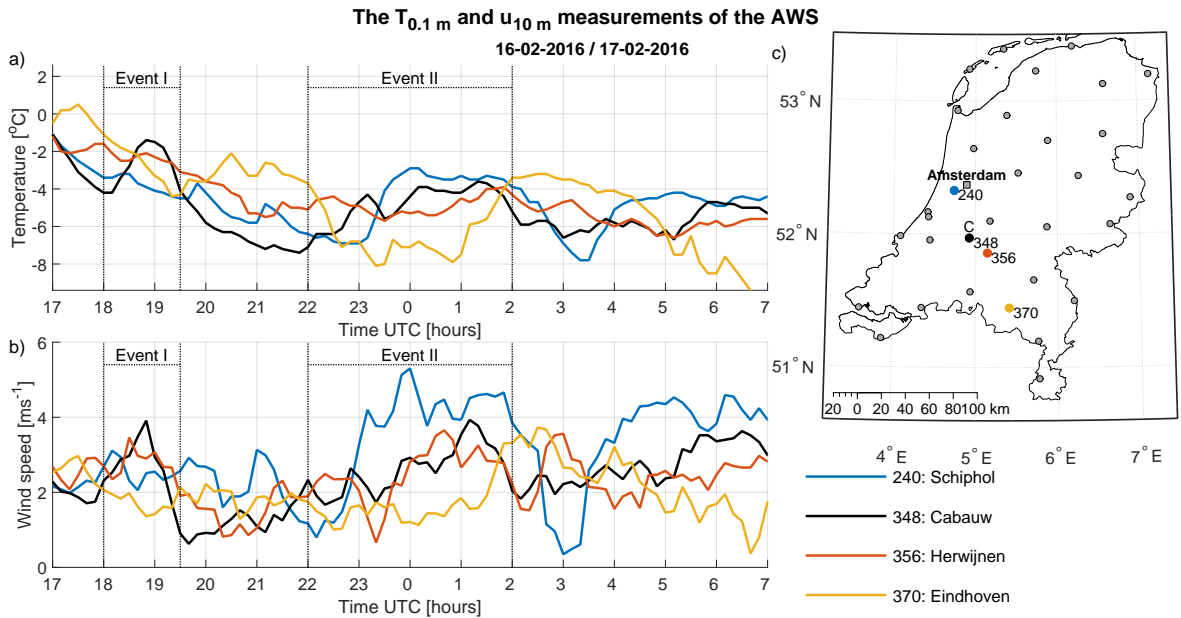

Figure 4.2: The $T_{0.1m}$ (a) and u_{10m} (b) observations on the night of the 16th to the 17th of February 2016, as well as the location of the AWS (c). The stations AWS260 (De Bilt), AWS269 (Lelystad), AWS344 (Zestienhoven) and AWS348 (Cabauws) form the first line for the cross method, used to study the size and propagation direction of the turbulent structures observed at Cabauw. The first burst of turbulence around 19:00 UTC is found by three out of four stations. Only AWS344 does not show a clear turbulent bursts with similar characteristics. The second turbulent event, between 22:00 and 2:00 UTC, is not clearly visible in the other stations. AWS344 shows a very clear signal in both parameters between 23:00 and 3:00 UTC. The other stations show a more gradual increase in u_{10m} which is not always visible in the $T_{0.1m}$ measurements.
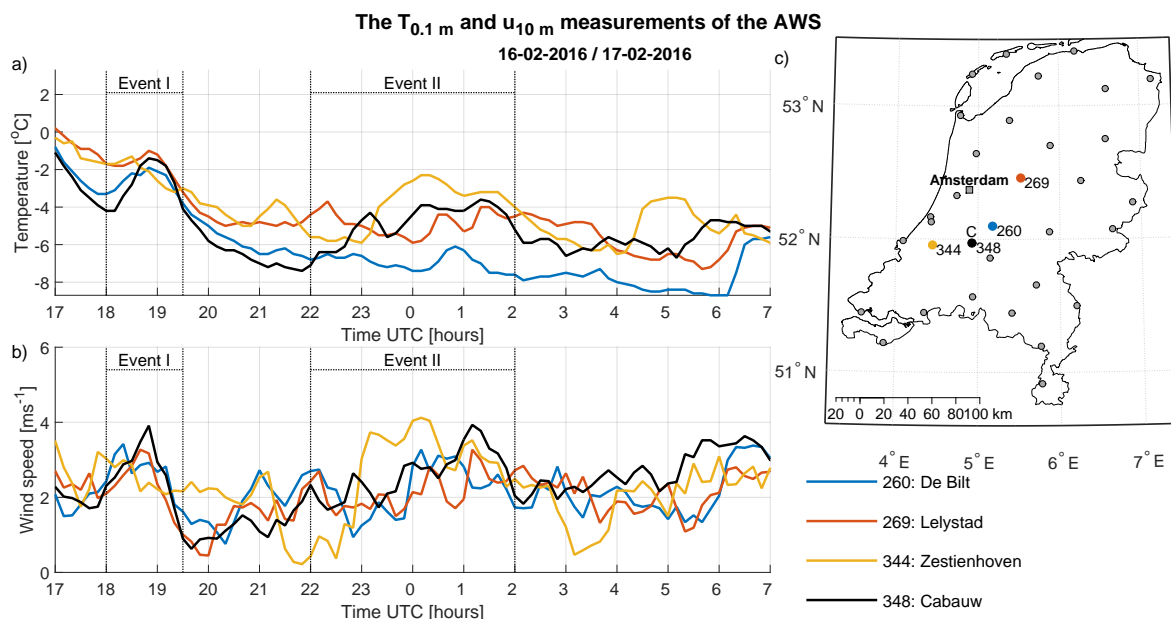
Figure 4.3: The $T_{0.1m}$ (a) and u_{10m} (b) observations on the night of the 16th to the 17th of February 2016, as well as the location of the AWS (c). The stations AWS240 (Schiphol), AWS348 (Cabauw), AWS356 (Herwijnen) and AWS370 (Eindhoven) form the second line for the cross method, used to study the size and propagation direction of the turbulent structures observed at Cabauw. The first turbulent burst around 19:00 UTC is only found in the u_{10m} measurements of AWS352. The main features of the second turbulent signal, between 22:00 and 2:00 is found at all four stations in both parameters with some differences in the characteristics of the signal.

Observations of the ('horizontal') red transect of the cross method (figure 3.8) are shown in figure 4.3. Multiple stations in this figure observe a turbulent event with similar characteristics as the first turbulent event at Cabauw. Both AWS260 and AWS269 show a strong increase in both $T_{0.1m}$ and u_{10m} between 18:00 and 19:30 UTC. Around this time, AWS344 observes less distinct fluctuations that have different characteristics than the turbulent event at Cabauw. When studying the first event at Cabauw, no relation was found with observed turbulence at the stations neighbouring the ones in 4.3.

Turbulence is found at all stations in figure 4.3 around the time of the second turbulent event at Cabauw; between 22:00 and 2:00 UTC. However, the turbulence has different characteristics at all four stations. For example, u_{10m} more or less steadily increases at Cabauw from 22:00 to 1:00 UTC, while u_{10m} fluctuates with an amplitude of approximately 1.5 ms^{-1} at AWS260. Between 22:00 and 2:00 UTC, no clear relation was found between any of these four stations.

The fact that this turbulent event is observed at multiple stations allows for studying propagation of the structure. The first turbulent event is only observed in the ('horizontal') red transect of the cross. As a result, only propagation parallel to this line can be inferred from the observations. The u_{10m} observations are analyzed to find a phase shift, i.e. a time delay between one station experiencing the turbulent event compared to another station. The propagation direction of the structure can be inferred from this phase shift. No clear phase shift was found between these three stations, as shown in figure 4.3. Therefore, no clear propagation of this structure is observed.

The three stations which observe this event are located on a 68 km long line from southwest to northeast. This indicating an elongated shape of the turbulent structure. Based on this distance between the stations, the length of the structure is estimated to be a minimum of 68 km.

4.2. Discussion

A relation in turbulence bursting characteristics is rarely found between Cabauw and one or more neighbouring stations. This is illustrated by the first case, the night of the 14th to the 15th of April 2015. In this example, short-lived turbulence is observed at all three stations in figure 4.1. However, there was no direct relation found between the turbulence at the stations. The conditions at these stations are suitable for short-lived turbulence, but the turbulent structures are not sufficiently large to span over multiple stations.

While this is true for most cases that were analyzed, one exception was found. The second case, the night of the 16th to the 17th of February, does show relation in turbulence bursting characteristics between stations, as shown in figure 4.2 and 4.3. The first strong turbulent burst at Cabauw, between 18:00 and 19:30 UTC, is clearly found at the two stations northeast of Cabauw. Two other stations, AWS344 (west of Cabauw) and AWS356 (south-east if Cabauw), observe a weaker turbulent event around the same time.

When studying the second event of the second case, both AWS240 (figure 4.2 and AWS344 (figure 4.3) observe a strong turbulent event with similar characteristics. The two stations show a large increase in both $T_{0.1m}$ and u_{10m} between 22:30 and 3:00 UTC. As discussed in section 2.1, turbulent mixing increases, indicated by the increased u_{10m}, strongly increases the near-surface temperature during this time period.

To study this structure, stations west of AWS344 and AWS240 are studied. Figure 4.4 shows the $T_{0.1m}$ (a) and u_{10m} (b) observations of stations AWS215, AWS240, AWS330 and AWS344. Stations further to the north or south do not observe this structure. AWS210 is not considered here, because the observations of this station are very similar to those of AWS215. Note that u_{10m} observations of AWS330, located at the coast, exceed the scale of the graph. The latter is limited to 6 ms^{-1} for clarity reasons.

All these stations show a very similar signal between 22:00 and 3:00 UTC, except for AWS330. The higher wind speed is most likely a result of its location near the coast. Still, this station observes a very similar turbulent signal in both parameters to the other stations, even though the high wind speeds indicate continuous turbulent conditions. As such it is likely that the turbulent event is caused by a large scale non-stationary forcing, rather than by internal dynamics (that is in spite of the data selection procedure that was aimed at avoiding such cases).

Propagation of this structure is analyzed by studying the phase shift of the turbulent signal. AWS330 experiences the increase in both parameters first, followed by AWS215, then by AWS344 and AWS240 at around the same time. This indicates that the structure came from the sea and moved to the east. The turbulent event is observed without phase shift over a distance of 46 km; the distance between AWS240 and AWS344. This implies that the turbulent structure spans a minimal distance of 46 km. This is different from the are area affected by the turbulent event, which results from the instantaneous size of the structure and its propagation.
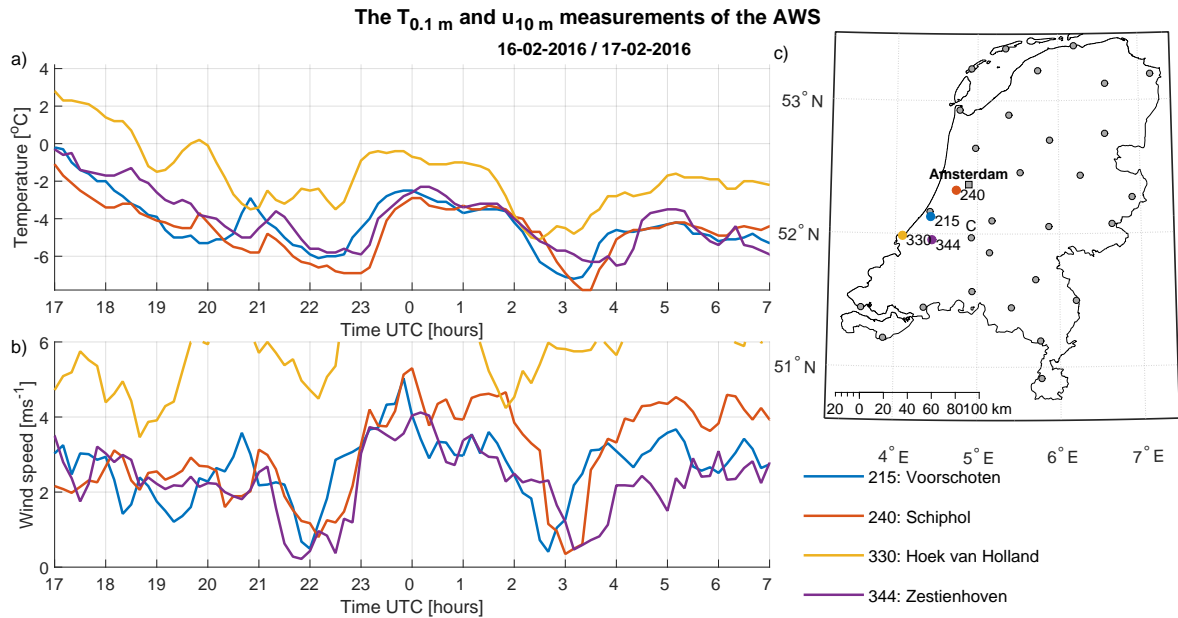

Figure 4.4: The $T_{0.1m}$ (a) and u_{10m} (b) observations on the night of the 16th to the 17th of February 2016, as well as the location of the AWS (c). The stations AWS215 (Voorschoten), AWS240 (Schiphol), AWS330 (Hoek van Holland) and AWS344 (Zestienhoven) are shown, because these stations show a large turbulent event between 22:00 ad 3:00 UTC, followed by a next increase in turbulence after 3:30 UTC. All stations show strong agreement in the $T_{0.1m}$ observations. In the u_{10m} observations, all stations but AWS330 show very similar observations as well. AWS330 is located directly at the coast, which is the likeliest explanation for the high wind speed. It still, shows increases in both parameters around the same time as the other stations. It is the first station to observe the structure, followed by AWS215, then by AWS240 and AWS344, which indicates propagation from west to east. The structure is only observed at these three locations, which span a distance of 68 km.

The largest distance between stations where the event is observed is 60 km, which gives an indication of the scale of the area affected by the turbulent event.

   In summary; there are large differences between the nights that were studied, but the turbulent structures found at Cabauw generally do not reach neighbouring stations. The only exception to this showed two very strong turbulent events that did span over multiple stations. This allowed for a rough first guess of the scale of these structures, bases on a visual analysis of the observations. It also indicates that it is possible for these structures to span over multiple kilometres and reach other stations.
   The main conclusion of the present analysis is that the turbulent structures are too small to be capture by the AWS network. As a result, the station correlation method (section 3.5) is not applied to this network. No conclusive answer can be given to the first research question (RQ 1), based on observations of the AWS network. A denser network is required to estimate the spatial scale of short-lived turbulent structures and answer this research question.

Analysis of the Schiphol Airport network

It was concluded in chapter 4 that the AWS network is too sparse to capture short-lived turbulent structures. However, the results do give indication that these structures may span up to several kilometres. It is expected that the much denser Schiphol Airport network is able to capture the structures and that high correlations will be found between multiple stations. Note that, observations from the Schiphol Airport network have a temporal resolution of one minute. Combined with the short distance between the stations, this high temporal resolution allows for a more detailed analysis of the observations.

The spatial scale of short-lived turbulent structures is discussed in section 5.1. Using the same approach as in chapter 4, the presence of strong correlation between multiple stations is first confirmed by visual analysis. Only then is the station correlation method applied to quantify the correlation and relate it to the distance between the stations. From this, the spatial scale of the short-lived turbulent structures can be estimated. First, the results are described in subsection 5.1.1, using two exemplary cases. Secondly, the validity of the method and the implications of the results are discussed in section 5.1.2.

Additionally, large regional temperature variations in the SBL are found in these network observations. This is discussed separately in section 5.2, where two cases are studied. These nights present interesting examples of regional temperature variations in the nocturnal boundary layer.

5.1. Spatial scale of short-lived turbulent structures

This section discusses the spatial scale of short-lived turbulent structures. The results are discussed first in subsection 5.1.1. Observations of two cases are shown: the night of the 16th and 17th of February 2016 and the night of the 10th and 11th of December 2013. For both cases, the results of the visual analysis and the station correlation analysis are shown. A intense turbulent event is studied in detail in the first case. The second case provides an example of a much smaller turbulent event. The second case is an example of a small turbulent structure. At the end of the subsection, results are summarized in a table. The implications of these results are discussed in section 5.1.2, where recommendations for future studies on the topic are given as well.

5.1.1. Results

The analysis of the first case, also discussed in chapter 4, focusses only on the largest turbulent event of the night, as shown using the analysis window in figure 5.1. This figure shows the $T_{0.1m}$ (a) and u_{10m} (b) observations and the locations of the three stations on the map (c). Events outside the analysis window are not part of that turbulent event and are not considered in the station correlation method.

The u_{10m} observations show that all three stations do observe the turbulent event around midnight, but that there are differences in characteristics. AWS240.01 and AWS240.24 experience the event almost simultaneously, over a relative distance of 12 km. The u_{10m} observations at both stations show a strong increase at 22:00 UTC, followed by two distinct peaks and a large drop around 2:00 UTC. The correlation between the $MAWF$ signals of these stations is high at 0.73. AWS240.22 is located 21 km east of AWS240.01 and observes the u_{10m} increase about an hour later. The u_{10m} observations also do not share the two characteristic peaks. The drop-off after 2:30 UTC is weaker as well compared to the other two stations. While both stations most
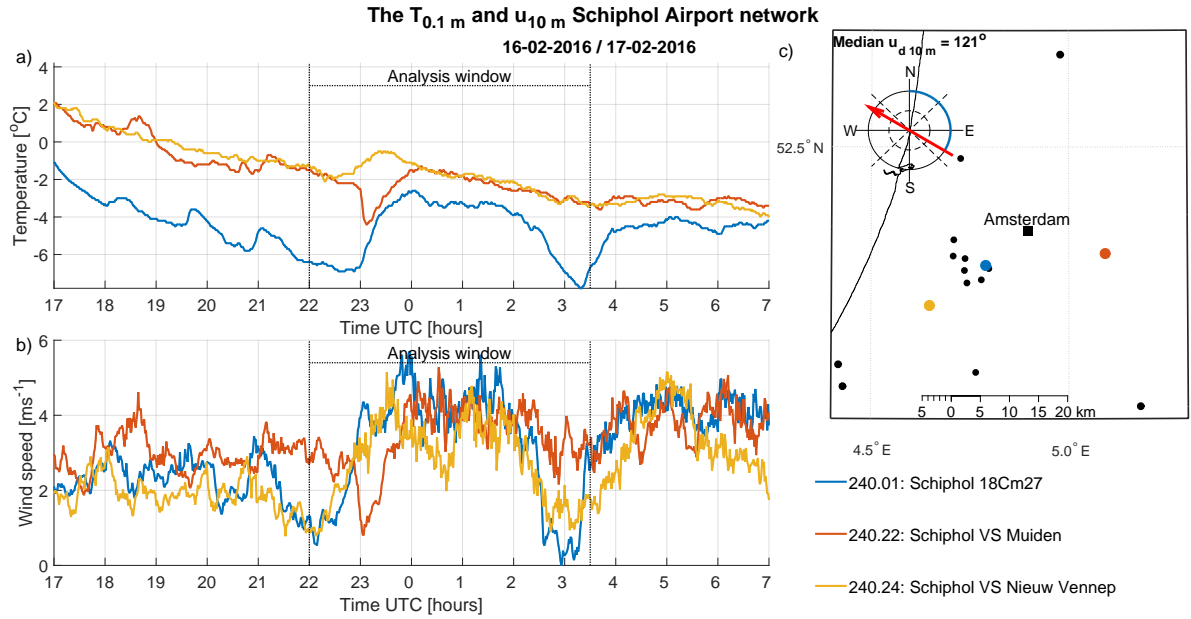
The $T_{0.1\,m}$ and $u_{10\,m}$ Schiphol Airport network
16-02-2016 / 17-02-2016

Figure 5.1: The $T_{0.1m}$ (a) and u_{10m} (b) observations on the night of the 16th and 17th of February 2016, as well as the location of the AWS with the median u_{d10m} at the airport (c). The time series of the turbulent event is shown in the analysis window. AWS240.01 and AWS240.24 both observe the turbulent event and their u_{10m} observations are highly correlated. Correlation between AWS240.01 and AWS240.22 is weak, as it observes the event with a delay of an hour and with different characteristics. The $T_{0.1m}$ observations increase with the u_{10m} observations for AWS240.01 and AWS240.22, but only a low response is observed at AWS240.24.
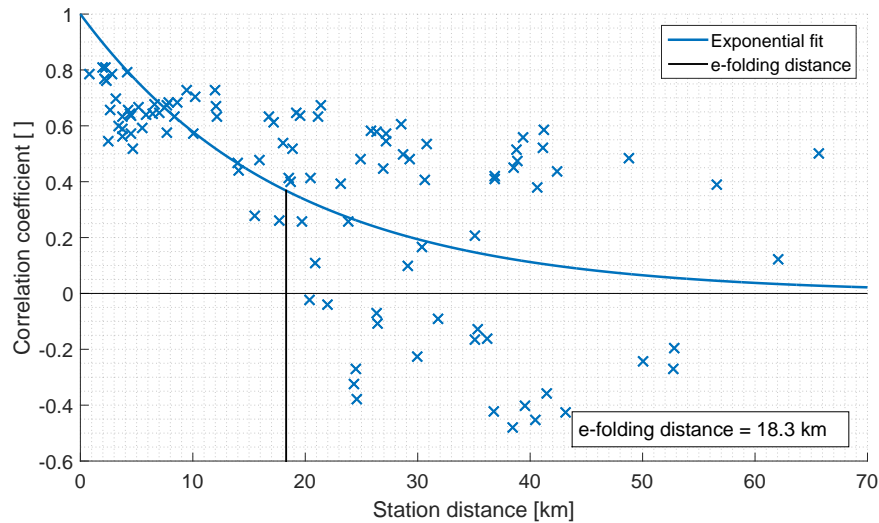

Figure 5.2: The results of the station correlation method of the night of the 16th and 17th of February 2016. It shows a scatter diagram of the station distance against the correlation coefficient of the time series within the analysis window between all station combinations. An exponential fit to the data is shown in blue. The e-folding distance (black) is used to estimate of the spatial scale of the structure to be 18.3 km.

likely experience the same event, the differences between AWS240.01 and AWS240.22 result in a correlation coefficient of 0.11.

The increase in u_{10m} at AWS240.01 is accompanied by an increase in $T_{0.1m}$. This a consequence of warm air from higher altitude being transported towards the surface by turbulent mixing, as shown in figure 2.2. Turbulence is sustained until 3:00 UTC, as is indicated by the u_{10m} decrease. At that time, turbulence is suppressed by buoyancy again (equation 2.5). Without turbulent mixing, $T_{0.1m}$ decreases by radiative cooling, as can be seen at AWS240.01 in figure 5.1.

The $T_{0.1m}$ observations are different for the three stations. Where AWS240.01 shows a significant increase during the event, this increase is much weaker at the other two stations. At AWS240.22, a sharp decrease in

$T_{0.1m}$ is found just before the event. This drop coincides with the decrease in u_{10m} and indicates a sudden lack of turbulent mixing. The $T_{0.1m}$ at AWS240.24, shows a much lower response ($< 2^oC$) to the increasing u_{10m}.

Using the $MAWF$ time series within the analysis window (not shown), the station correlation method relates station distance to the correlation coefficient, as shown in figure 5.2. Overall, high correlation is found for stations that are less than 13 km apart. For larger distances significant correlation is found as well, but the number of poorly correlated stations increases. As a result the spread of these correlation points increases with distance. Using the exponential fit of figure 5.2, the e-folding distance (black) is determined to be 18.3 km. This appears to be in agreement with an early estimate based on the visual analysis, of which an example is shown in figure 5.1.

It should be noted however, that the exponential fit appears to be a poor model of the data. A reason for this discrepancy could lie in the fact that this method assumes the underlying process to be isotropic in space, i.e. correlation only depending on absolute distance. It is likely that the turbulent structure is non-isotropic in reality. This means that the correlation depends not only on distance, but on direction as well.

A map of the correlation coefficients between stations can be used to study the assumption of isotropy in the station correlation method. Figure 5.3 is such a map, showing correlation between all stations and a single reference station. AWS240.14 is chosen as the reference station because of its position in the center of (dense core of) the network. The correlation coefficients between this reference station and other stations are shown from 0 (white) to 1 (red) with linear interpolation between stations.

The results in figure 5.3 suggests a more or less elliptical shape of the structure, with its semi-major axis in north north-east direction. The fact that the correlation coefficient is significant at AWS215 (far southwest of Schiphol Airport) and AWS240.21 (north of Schiphol Airport) suggest that this semi-major axis is longer than their spatial separation of 41 km. This is significantly larger than the e-folding distance. The e-folding distance seems to correspond with the length of the semi-minor axis of the structure. The network however, is not suitable for an accurate estimation of the shape and size of the structure. While the linear interpolation
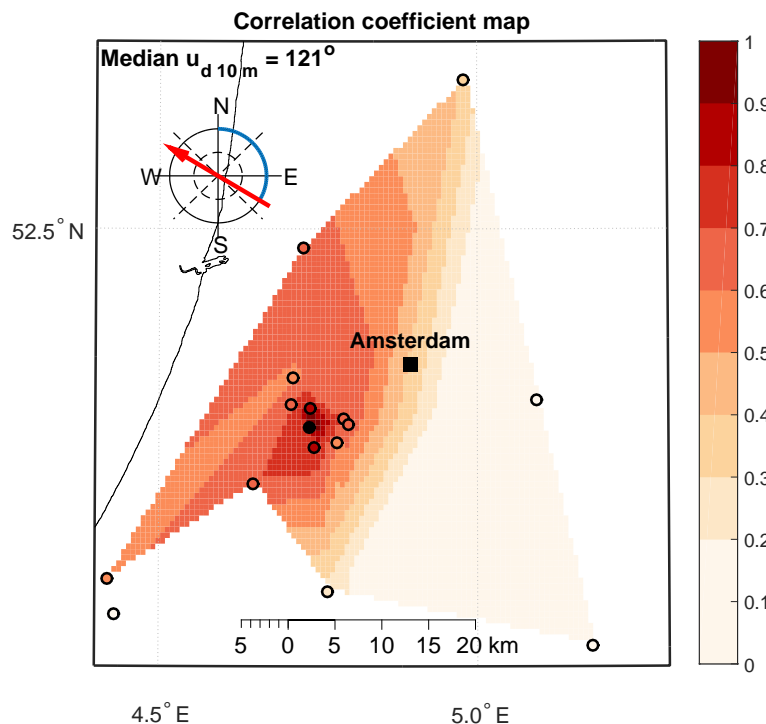

Figure 5.3: The correlation coefficients between AWD240.14 and the other stations in the Schiphol Airport network. Significant correlation is found west of Schiphol Airport while the stations in the east are weakly correlated. This difference in correlation coefficient at similar distance is also found in the results of the station correlation method shown in figure 5.2. This map also gives an idea about the shape of the structure, which seams to be more or less elliptical with a semi major axis in north north-east direction.

between stations gives an idea of the shape and size, it cannot be relied upon for an accurate estimation. The stations in the Schiphol Airport network are spaced unevenly outside the airport itself and distances can be large between stations.

The figure not only gives a rough idea about the shape of the structure, it also gives an explanation for the spread that is found in scatter diagram of figure 5.2. West and north of Schiphol Airport, correlation is high. Correlation is weak east of the airport, even though the distances between stations on the east and west are similar. Besides spatial separation of the stations, direction also plays an important role. It is noteworthy that the median direction of the u_{d10m} is nearly perpendicular to the semi-major axis of the structure, indicating a relation between wind direction and the shape of the structure. This will be discussed further when propagation of the structure is discussed, but note that this relation is not found for other cases.

The phase shift in the observations of this intense turbulent structure is already described in section 4.2 and shown in figure 4.4. Similar results are found in figure 5.1 between AWS240.01 and AWS240.22 and in visual analysis of other stations (not shown). This phase shift indicates propagation of the structure in east-southeast direction. The near-surface wind speed u_{d10m} is nearly constant for all three stations in figure 5.4, only changing when u_{10m} is very low. The wind direction is approximately 120°, coming from the east-southeast, which is opposite to the propagation direction of the structure.

In section 4.2, it was indicated that the turbulent event could result from large scale non-stationary forcing. The fact that the semi-major axis is perpendicular to the propagation direction and that the structure is not driven by the near-surface wind strengthens this idea. The synoptic weather map at midnight is used to validate this theory. In figure 5.5, a high pressure area is found east of the Netherlands and a low pressure area in the west. The system moves roughly from west to east, shown with a green arrow, in approximately the same direction of the propagation of the structure. It is therefore concluded that this turbulent event is indeed a result of large scale non-stationary forcing.
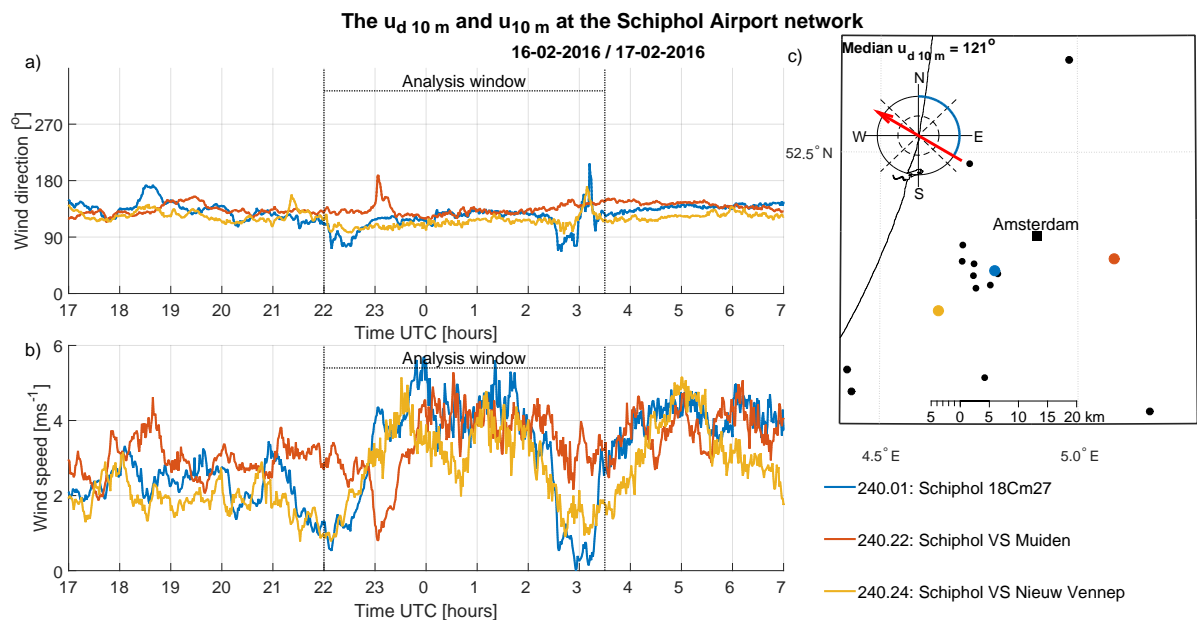

Figure 5.4: The u_{d10m} (a) and u_{10m} (b) observations on the night of the 16th and 17th of February 2016, as well as the location of the AWS with the median u_{d10m} at the airport (c). The time series of the turbulent event is shown in the analysis window. AWS240.01 and AWS240.24 both observe the turbulent event almost simultaneously. AWS240.22 observes the event after a delay of about an hour and with different characteristics. All three stations observe a near constant u_{d10m} of approximately 120^oC (west-northwest direction), only changing when u_{10m} is low. The observed delay at AWS240.22 and at other stations (not shown) indicate propagation of the structure in east-southeast direction.
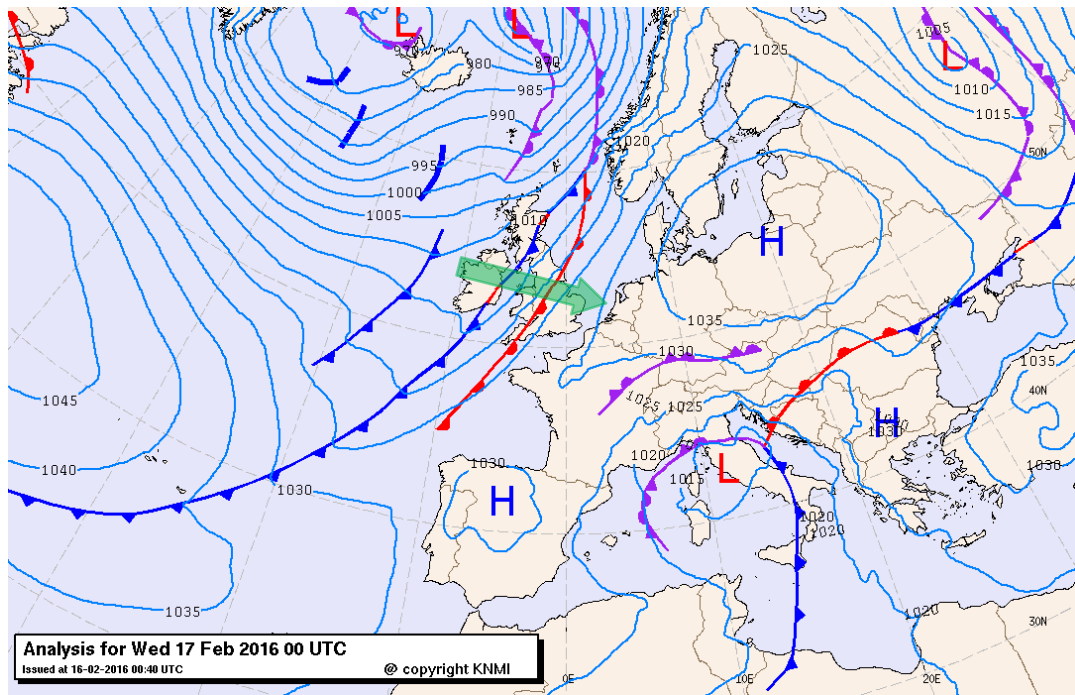
Figure 5.5: The synoptic weather map of the night of the 17th of February 2016 at 0:00 UTC. It shows a high pressure system over the mainland of Europe, which is moving in east north-east direction. A warm front moving towards the Dutch coast, in the direction of the green arrow. This front does not reach the main land on the 17th of February 2016.

The second case, the night of the 10th and 11th of December 2013, is an example with many small short-lived turbulent events. Figure 5.6 shows observations of three stations with small relative distances; 0.8 km and 2.6 km from AWS240.01 to AWS240.11 and AWS240.12 respectively. $T_{0.1m}$ observations are only shown for AWS240.01, as the two other stations are wind poles where no information on temperature dynamics is available. The analysis window captures the part of the time series encompassing the largest turbulent event.
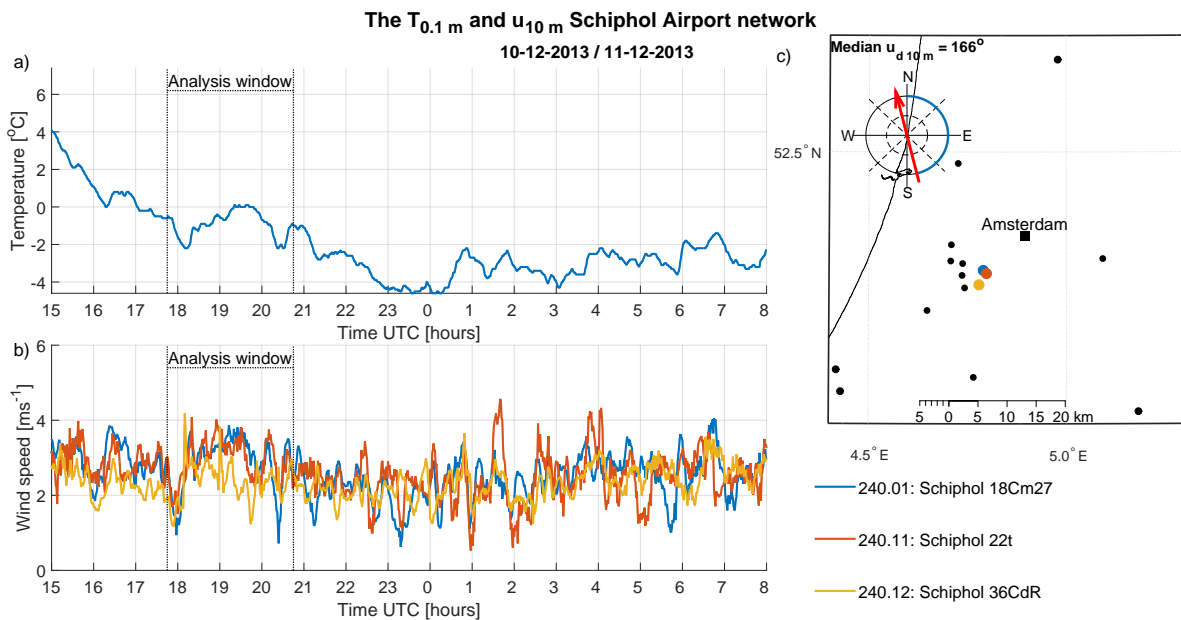

Figure 5.6: The $T_{0.1m}$ (a) and u_{10m} (b) observations on the night of the 10th and 11th of December 2013, as well as the location of the AWS with the median u_{d10m} at the airport (c). The analysis window encompasses the turbulent event. The u_{10m} of AWS240.01 and AWS240.21 observations are strongly correlated, but correlation between AWS240.01 and AWS240.12 is weaker.
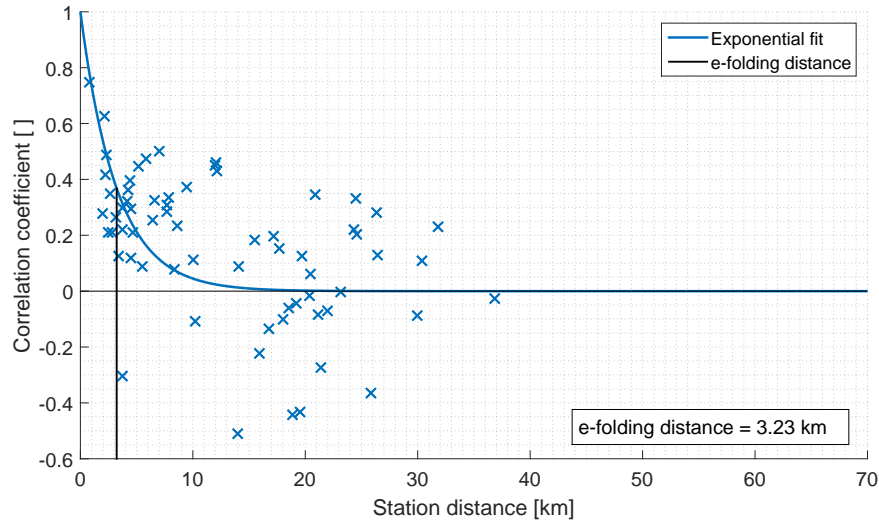
Figure 5.7: The results of the station correlation method of the night of the 10th and 11th of December 2013. It shows a scatter diagram of the station distance against the correlation coefficient of the time series within the analysis window between all station combinations. An exponential fit to the data is shown in blue. The e-folding distance (black) is used to estimate of the spatial scale of the structure to be 3.23 km.

The u_{10m} observations in figure 5.6b show that AWS240.01 and AWS240.11 observe very similar signals. The correlation between the $MAWF$ signals (not shown) of these stations is high at 0.75. At the onset of the event, u_{10m} observations at AWS240.12 show similarities with the other two. Later on however, the signal of AWS240.12 becomes very different. Consequently, the correlation coefficient between this station and AWS240.01 is lower at 0.35.

The station correlation method shows in figure 5.7 that only two sets of stations are highly correlated. These stations are AWS240.01 with AWS240.11 ($R = 0.75$) and neighbouring stations AWS240.15 and AWS240.16 in the west of the airport ($R = 0.63$). Based on the e-folding distance, the spatial scale of this structure is estimated to be 3.23 km.

The correlation decreases quickly with distance. For distances larger than the e-folding distance (3.23 km) a spread is found in the correlation coefficient, ranging from -0.5 to 0.5, as shown in figure 5.7. Contrary to the first case (figure 5.2), this spread is not a result of the shape of the structure. Figure 5.8 shows two stations which are moderately correlated with AWS240.01, but are located at distances of 4.4 km and 12 km respectively. The correlation coefficient between AWS240.01 and AWS240.24 is 0.45, but the u_{10m} observations are unrelated. The same is found between AWS240.01 and AWS240.13 where the u_{10m} are unrelated, but still results in an moderate correlation coefficient of 0.39. The likeliest explanation for the spread in figure 5.7 is noise., i.e. unrelated turbulent events found nearly simultaneously at different stations.
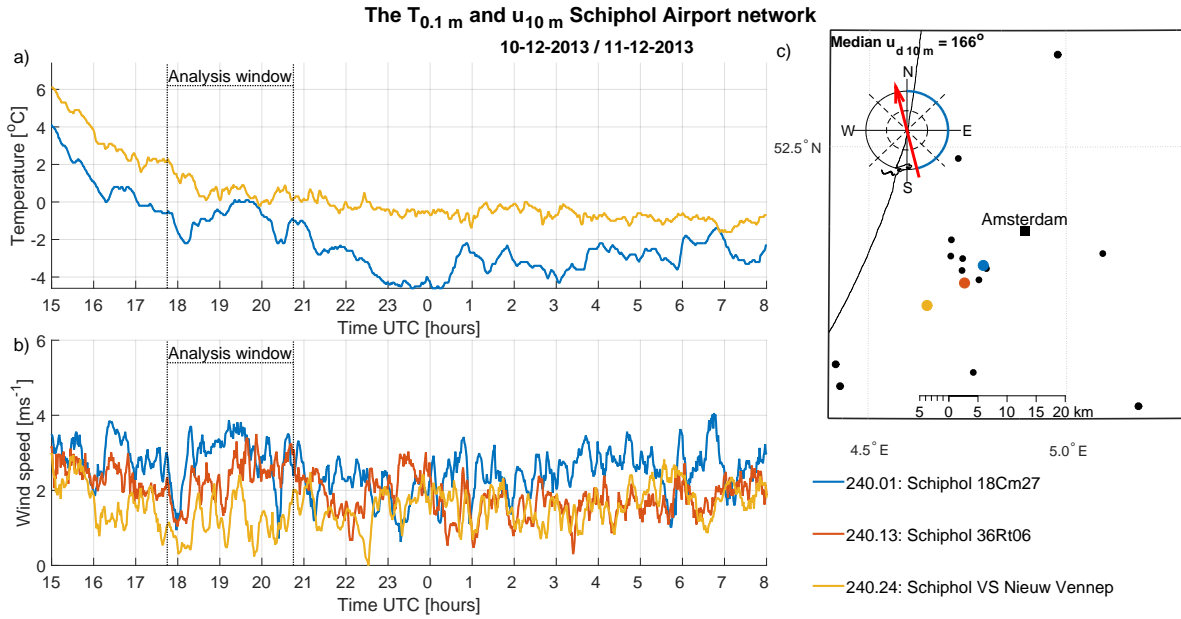
Figure 5.8: The $T_{0.1m}$ (a) and u_{10m} (b) observations on the night of the 10th and 11th of December 2013, as well as the location of the AWS with the median u_{d10m} at the airport (c). The time series of the turbulent event is shown in the analysis window. AWS240.01 and AWS240.21 observe the turbulent event near simultaneously and their u_{10m} observations are strongly correlated. Correlation between AWS240.01 and AWS240.12 is weaker, as AWS240.12 observes a different u_{10m} signal after the first 30 minutes of the analysis window. $T_{0.1m}$ responds strongly to changes in u_{10m} at AWS240.01. At AWS240.11 and AWS240.12, only u_{10m} observations are available.

Table 5.1: A list of the e-folding distances of all cases that were analyzed using observations of the Schiphol Airport network. Of each case, a single turbulent event is studied and the e-folding distance is calculated using the station correlation method.

Dates	Time Analysis window [UTC]	e-folding distance [km]
10-12-2013 to 11-12-2013	17:45 to 20:45	3.23
03-07-2014 to 04-07-2014	00:45 to 02:15	8.61
17-03-2015 to 18-03-2015	23:30 to 03:30	2.21
23-03-2015 to 24-03-2013	20:00 to 02:00	9.97
14-04-2015 to 15-04-2005	21:45 to 00.15	1.39
19-04-2015 to 20-04-2015	00:00 to 02:30	14.19
06-08-2015 to 07-08-2015	01:00 to 04:00	24.11
31-10-2015 to 01-11-2015	02:00 to 03:45	8.93
17-01-2016 to 18-01-2016	22:15 to 00:30	8.26
16-02-2016 to 17-02-2016	22:00 to 03:30	18.30
12-04-2016 to 13-04-2016	22:00 to 01:30	15.42

Using observations from the Schiphol Airport network, the 11 cases from the final selection of section 3.3 (table 3.2) are analyzed in this study. Their respective e-folding distances are shown in table 5.1, as well as the time interval of the analysis window. Two more examples are shown in Appendix D, but these are not discussed in detail. The results of table 5.1 show that there are large variations between nights. The median e-folding distance is used as an estimate of the spatial scale of short-lived turbulent events in the Netherlands. The median is a more robust "average", which is less affected by a single very large/small event. The e-folding distances range between 1.39 km and 24.11 km, with a median of 8.9 km. Based on these results, the spatial scale of short-lived turbulent events is estimated to be 8.9 km.

5.1.2. Discussion

Visual analysis of this network is mostly used to confirm that short-lived turbulent structures span multiple stations. With that, the first research question (RQ 1) is answered: Short-lived turbulent structures can be observed using existing observational networks. It works well as a qualitative analysis method, as similar patterns in time series are easily recognized visually. It is not suitable for a quantitative analysis, but the

figures used for the visual analysis are also a powerful tool for validation of the station correlation method.

The station correlation method gives a quantitative analysis of the scale of short-lived turbulent structures. This method only returns high correlation for stations that observe the turbulent structure (near) simultaneously. Negative correlation indicates propagation of the structure. However, it is the scale of the structure itself, not area affected by the turbulent structure, that is the focus of this study. Using the e-folding distance, an more objective and quantitative estimate of the scale of the structures is made. The e-folding distance consistently estimates the distance at which weakly correlated stations are first found.

Using the e-folding distance as an estimate for the scale of the turbulent structure assumes spatial isotropy of the structure and the underlying processes. The validity of this assumption is studied using the scatter diagram of the method and a correlation map. Anisotropy can be inferred from the spread in the scatter diagram of the station correlation method, since that is either caused by noise or an anisotropic structure. Noise is found in the scatter diagram as moderate correlation ($0.3 < R \leq 0.5$), both positive and negative, for distances larger than the e-folding distance, as shown in figure 5.7. An anisotropic structure results in both high correlation ($R > 0.5$) and low correlation in the scatter diagram for distances larger than the e-folding distance, as shown in figure 5.2.

A correlation map, as shown in figure 5.3, is used to resolve the question of the validity of the assumption of isotropy. This map only gives a rough impression of the shape of the structure, due to the limitations of the network. The network has a dense core at the airport, but stations outside the airport are spaced unevenly and distances between stations can be large. This leaves large gaps in the spatial coverage, e.g. northeast and southeast of the airport. This is the main weakness of the network and the answer to the fifth research sub-question (RsQ 5). As a result, an accurate estimation of the shape of the structure cannot be inferred from the figure. This also prevents an in-depth two-dimensional analysis of the turbulent structure.

While the network is limited, the rough impression, in combination with the scatter diagram, is sufficient to conclude anisotropy for large structures, as was done for the first case. As a rule of thumb, the one-dimensional estimation using the e-folding distance is comparable to the semi-minor axis of an elliptical structure. Consequently, the assumption of isotropy underestimates the spatial scale of anisotropic turbulent structures.

Considering the fourth research sub-question (RsQ 4), this shows that the method has a major weakness. The e-folding distance alone is not an accurate estimate of the scale for spatially anisotropic structures. The scale of these structures is underestimated with the station correlation method. For turbulent structures which are spatially isotropic (e.g. figure D.1 in Appendix D), the assumption is valid and the method gives a valid estimation of the spatial scale of the structures.

The first case, the night of the 16th and 17th of February 2016, shows clear propagation of the turbulent structure. Propagation of this structure is discussed in section 4.2 as well. Both figure 4.4 and 5.1 indicate propagation in east-southeast direction, which is opposite to the near-surface wind direction. The semi-major axis of the structure is perpendicular to u_{d10m} and to the propagation direction, indicating a relation between either/both these factors and the shape of the structure. However, this event is likely to be a result of large scale non-stationary forcing. No clear propagation was found in the other ten cases. The conclusions on propagation, drawn from this single case, are therefore not necessarily representative for turbulent events caused by internal system variability. A future network, with evenly spaces stations is required to study structure propagation in the future.

All 11 cases, analyzed using the Schiphol Airport network, show multiple turbulent events. The results of the station correlation method, shown in table 5.1, range from 1.39 km to 24.11 km with a median of 8.9 km. This answers the second research question (RQ 2): the spatial scale of short lived-turbulent structures in the nocturnal boundary layer is estimated at 8.9 km. Although a footnote is required, that this cloud be an underestimation in the case of spatially anisotropic structures.

The results confirm that the spacing of the AWS network, with an average station distance of 32.5 km, is too sparse to capture the short-lived turbulent structures. Note that only the clearest events are studied, based on the visual analysis. This manual selection of clear events results in a bias for large turbulent structures, as seen in figure 5.6 of the second case. The resulting estimate of the spatial scale can therefore be considered as the upper limit of the scale of short-lived turbulent structure.

The large structures are captured well by the network, but the assumption of isotropy can result in an underestimation of the spatial scale. The smaller structures (e-folding distance smaller than 5 km) have a

scale in the same order of magnitude as the distance between neighbouring stations at the airport (about 2 km). High correlation is only found between a few (1 or 2) pairs of stations for these structures. While this gives an indication of the spatial scale of the structures, the Schiphol Airport network is not sufficiently dense to accurately estimate the spatial scale of these smaller structures.

The range of e-folding distances of table 5.1 holds valuable information for the design of a future network to accurately capture short-lived turbulent events in the nocturnal boundary layer. Based on the estimates resulting from this study, a network with a dense core is recommended. To accurately capture the smaller structures of this study, with distances between stations no larger than 1 km. Surrounding the core, rings of stations with increasing relative distances (e.g. 2 km to 5 km) are recommended to capture the larger events. A network spanning a distance of at least 25 km is expected to be sufficient to capture the largest turbulent structures found in this study.

The main weakness of the Schiphol Airport network, sparse and unevenly spaced stations outside the airport, is a valuable source of information for future networks. This limits the possibilities to analyze the shape and propagation of the structures. A future network would be significantly improved by even spacing between (the layers of) stations and uniformity of the network area. These recommendations for a future network answer the third and final research question (RQ 3) on the network design required for an in-depth study on short-lived turbulent structures in the nocturnal boundary layer.

5.2. Regional temperature variations in the nocturnal boundary layer

Large temperature differences are found over relatively small distances, as is shown in the example of figure 5.9a. This figure shows the time series of the $T_{0.1m}$ (a) and u_{10m} (b) observations as well as the location of the three stations with the median u_{d10m} at the airport (c).

Temperature differences of 7^oC or larger are found in clear sky conditions between AWS240.02 and AWS260, which are located 43 km apart. The largest difference, 8.9^oC, is found just after 22:00 UTC. Only small u_{10m} differences between the three stations are observed during the night. The regional temperature variations can be a result of local conditions at each station, like e.g. soil properties and surrounding vegetation or buildings. This is outside of the scope of this study, but these results show that the impact is potentially significant.

Clouds can be a cause of regional temperature variations. As indicated in section 2.1, the direct effect
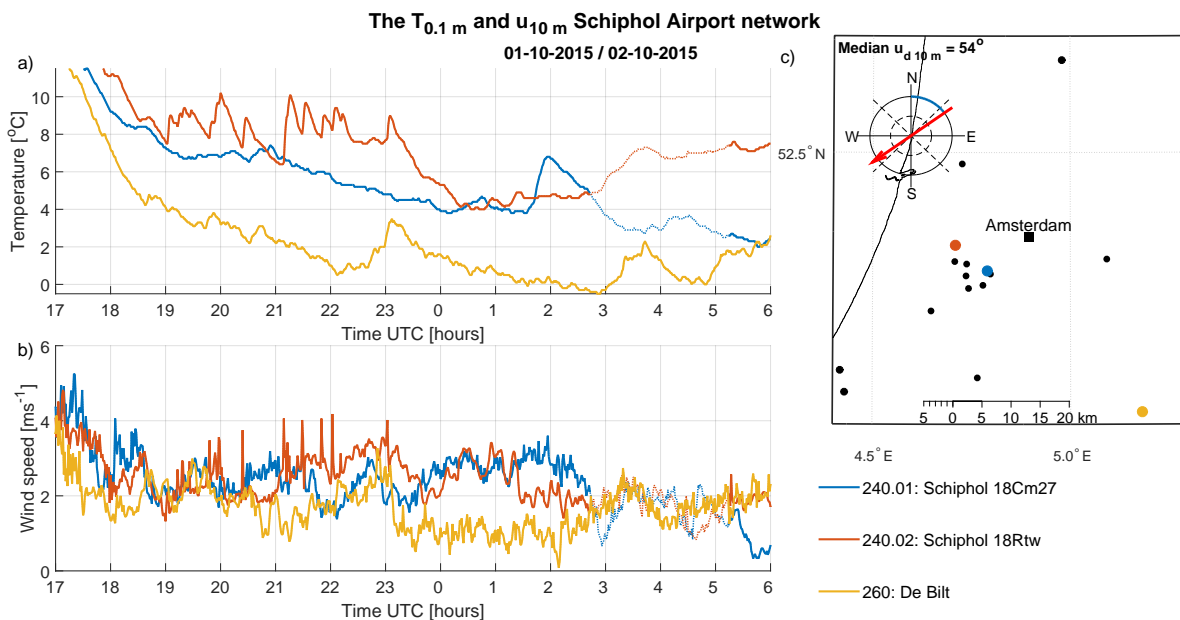

Figure 5.9: The $T_{0.1m}$ (a) and u_{10m} (b) observations on the night of the 1st and 2nd of October 2015, as well as the location of the AWS with the median u_{d10m} at the airport (c). A $T_{0.1m}$ difference up to 4^oC is regularly found between AWS240.01 and AWS240.02, from 19:00 to 23:30 UTC. The largest differences are found between AWS240.02 and AWS260, with a maximum of 8.9^oC. The u_{10m} observations show only small differences between these stations, with the largest differences of about $2ms^{-1}$. Observations of clouds are indicated by a dotted line, increasing $T_{0.1m}$ by approximately 2^oC at 3:00 UTC.
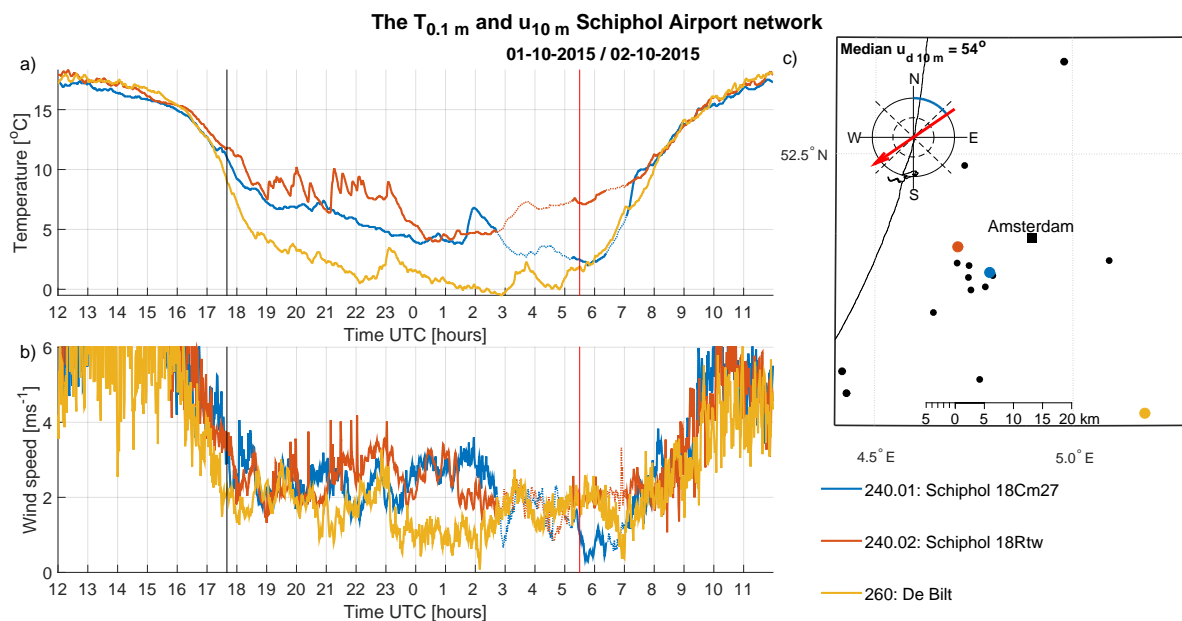
Figure 5.10: The $T_{0.1m}$ (a) and u_{10m} (b) observations on the 1st and 2nd of October 2015, as well as the location of the AWS (c). Sunset and sunrise are shown with a black and red vertical line respectively. Observation of clouds is indicated with a dotted line in the observations. Stations AWS240.01, AWS240.02 and AWS260 are shown, because the observed $T_{0.1m}$ differences are remarkable. During the day, the $T_{0.1m}$ differences between all three stations are about 1^oC. During the night, large differences are observed, up to a maximum of 8.9^oC between AWS240.02 and AWS260. The only differences in the observations between these two stations is a small difference in u_{10m} during the night. During the day, u_{10m} is high for all stations, indicating strong turbulence.

of clouds can locally increase the near-surface temperature. Around 3:00 UTC, a cloud is detected over AWS240.02, indicated by a dotted line. Observations of u_{10m} are nearly identical for both stations and turbulence is weak. It is therefore concluded that clouds increases $T_{0.1m}$ at AWS240.02 with about 2^oC and causes a $T_{0.1m}$ difference of 4^oC, between AWS240.01 and AWS240.02.

Local turbulence is another factor which can locally increase the near-surface temperature. In figure 5.9, AWS240.02 observes multiple turbulent events, as indicated by the multiple simultaneous increases in both u_{10m} and $T_{0.1m}$. This increases the temperature by about 4^oC and keeps it high for nearly 3 hours. No other potential causes for an increase in $T_{0.1m}$, e.g. clouds or changes in wind direction (not shown), are found. Turbulence is weak at AWS260, until around 23:00 UTC. A short-lived turbulent event increases $T_{0.1m}$ and reduces the difference with AWS240.01 from 4^oC to 1^oC, as turbulent mixing transports heat towards the surface, highlighting the impact local turbulence can have.

The regional temperature variations during the night are remarkable when compared to the daytime situation, as shown in figure 5.10. In this figure, sunset and sunrise are shown with a vertical black and red line respectively. During the day, the differences in near-surface temperature typically remained less than 0.5^oC. The u_{10m} observations are also high during the day, indicating turbulent mixing by convection. Figure 5.10 clearly shows the transition from a continuously turbulent convective mixed layer (unstable conditions) to a stable boundary layer (stable conditions), as illustrated in figure 1.1 and described in chapters 1 and 2. Turbulence weakens a few hours before sunset, because the sun stops heating the surface and convection dies out. As a result of the aforementioned local processes, large regional $T_{0.1m}$ differences up to nearly 9^oC are found during this night. Similar results are found in other nights (not shown), showing the general validity of this example. It highlights that it is challenging to make an accurate prediction of the nighttime temperature at a specific location. Local effects have a very large impact.

The four sharp increases in u_{10m} at AWS240.02, found between 21:00 and 22:00 UTC, are particularly interesting. These four peaks coincide with the times large airplanes (Boeing-747) take off from the Polderbaan runway, at which AWS240.02 is located. Artificial turbulence from airplanes appears to be the main cause of the local near-surface temperature difference between AWS240.01 and AWS240.02.

A clear example of the impact of a large airplane taking off is found on the night of the 29th and 30th of June 2015, shown in figure 5.11. The u_{10m} is very low during this night, except at 0:45 UTC, when a large
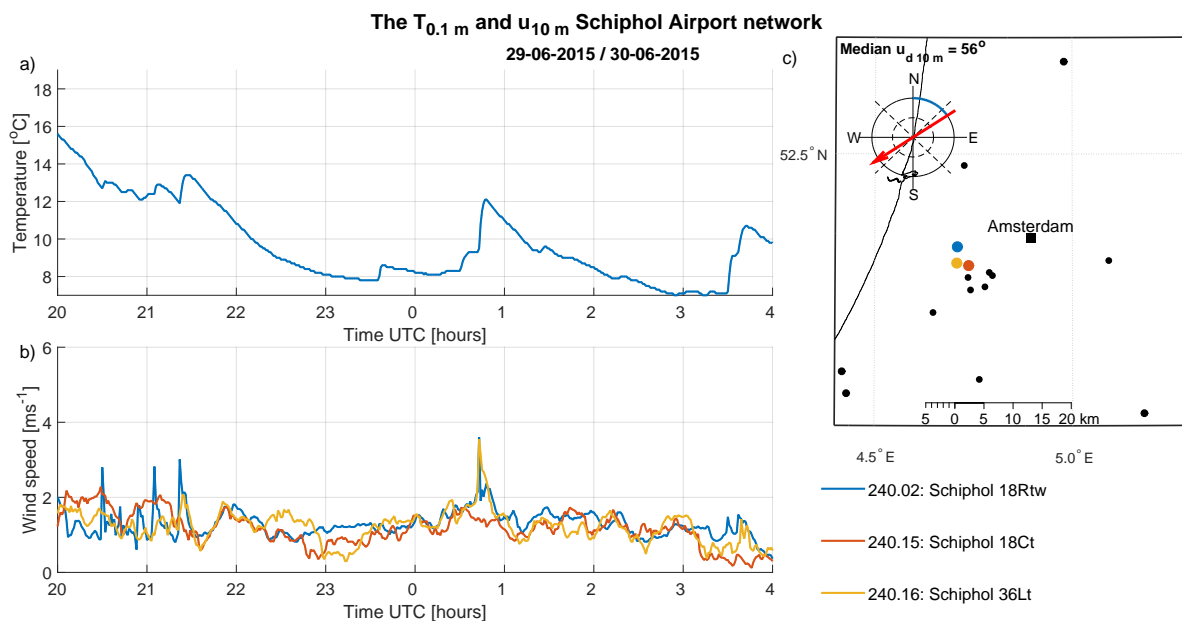
Figure 5.11: The $T_{0.1m}$ (a) and u_{10m} (b) observations on the night of the 29th and 30th of June 2015, as well as the location of the AWS with the median u_{d10m} at the airport (c). AWS240.02 and AWS240.16 are located at the north and south side of the Polderbaan runway, and AWS240.15 is the closest station to this runway. The wind speed is very weak for most of the night, except around 0:45 UTC, where AWS240.02 and AWS240.16 observe a large and very short increase in u_{10m}. The temperature responds strongly with an increase of $4^{o}C$. The time of this spike coincides with the take off of a Boeing-747 airplane. AWS240.15 does not observe this event.

increase in both parameters is observed. This large spike is only observed at AWS240.02 and AWS240.16, located at the north an south side respectively of the Polderbaan runway. The time of this turbulent burst coincides with a Boeing-747 airplane taking off from that runway. No such event is observed at AWS240.15, located nearby next to another runway. All three stations are placed at a distance of 105 m from the centreline of a runway.

The increase in u_{10m} is caused by the turbulent wake of the airplane. The burst only lasts for about a minute at AWS240.02. At AWS240.16, a slower u_{10m} decrease is observed, which can be explained by the wind direction. The u_{d10m} is directed to the southwest. Consequently, the wind pushes the turbulent wake towards this station. The $T_{0.1m}$ increases with about $4^{o}C$, simultaneous with the u_{10m} increase. The temperature jump is expected to be caused by turbulent mixing, but could be affected by heat from exhaust fumes of the airplane as well. The single event affects the $T_{0.1m}$ for more than an hour. The slope of $T_{0.1m}$ is similar to the slope at 20:00 and at 22:00 UTC, indicating that radiative cooling is the only process affecting the near-surface temperature after the event.

Only large airplanes (Boeing-744) are recovered in the wind and temperature signals in the observations. The landing of a plane, or a smaller plane taking off, is only rarely found when u_{10m} is already lower than $1ms^{-1}$. The effect of airplanes on the near-surface temperature shows potential for artificially creating turbulence to manipulate the surface temperature. The airplanes cause very short and intense bursts of turbulence, which are observed as sharp spikes lasting 1 or 2 minutes in the u_{10m} observations. A series of these bursts can increase the temperature significantly and it decreases at a much slower rate. This is shown in figure 5.9 between 21:00 and 23:00 UTC. This artificial turbulence is by-product of airplanes taking off, but it shows potential for intentionally and artificially creating turbulence to manipulate the near-surface temperature. This is an unintentional scientific finding of this study and will be studied in more detail in the future.

6

Conclusion

During clear nights with weak winds, there is little turbulent mixing between cold air near the ground and warmer air at higher altitude. This allows the temperatures close to the ground to decrease rapidly, which can lead to e.g. fog or severe frost events. Short-lived turbulent events can renew turbulent mixing, which significantly increases the surface temperature by mixing these warm and cold layers. Short-lived turbulence in the nocturnal boundary layer has been studied before by analyzing single tower observations, but so far, the horizontal spatial scale of this phenomenon is not known. This study aims to give first-order estimate of the spatial scale of short-lived nocturnal turbulent structures. It is a preliminary study, meant as an exploratory initiative as to assess the potential of the methodology for future in-depth research on this issue (using an observational network dedicated for this type of analysis). This objective, together with the scope of the project, leads to the following research questions (RQ):

RQ 1 *Can short-lived turbulent structures in the nocturnal boundary layer be observed using existing observational networks?*

RQ 2 *If so, what is the spatial scale of short-lived turbulent structures in the nocturnal boundary layer?*

RQ 3 *What network design is required for an in-depth study of short-lived turbulent structures in the nocturnal boundary layer?*

This study uses observations of wind speed and near-surface temperature from two existing observational networks in the Netherlands. Nights with short-lived turbulent events are selected by an automated filter and by manual selection. The criteria for the selection process are based characteristics of the very stable boundary layer regime and applied to observations from the Cabauw Observatory. The aim is to select nights with turbulence caused by the internal system variability rather than by cloud cover variability (which is considered to be a more trivial external factor). In total, 44 night (4% of the total amount) were selected, containing either cases with clear short-lived turbulent events, or edge cases with weak turbulence. From this subset, about ten nights are hand-picked for both networks to be studied in detail.

Note that this manual selection of clear short-lived turbulent events results in a bias for large turbulent structures. The resulting estimate of the spatial scale can therefore be considered as the upper limit of the scale of short-lived turbulent structure.

Each case is studied using a somewhat more subjective visual analysis as well as the more objective station correlation method. The visual method is used as a first filter as to identify turbulent mixing by visually studying near-surface temperature and the wind speed. Next, multiple stations in the network are visually compared find high correlation between stations. When correlation is found, the station correlation method is applied. Here, the correlation is quantified by calculating the correlation coefficient for every station pair using wind speed fluctuations during the turbulent event. A scatter diagram is made relating the distance between the stations to the correlation coefficient. An exponential fit is then made to this data and its e-folding distance is used as an estimate of the size of the structure.

First the automated weather station network of the KNMI is studied. The network contains 32 stations spanning the Netherlands, with an average distance of 32 km between neighbouring stations. Visual analysis

shows that turbulent structures are generally too small/incoherent in time to be recognized at multiple stations at different times. Nevertheless, a single counterexample is found, indicating that these structures can span multiple kilometres. A conclusive answer to the first research question (RQ 1) cannot be given, based on observations of the AWS network. A denser network is required to estimate the spatial scale of short lived turbulent structures.

Such a denser network is found at Schiphol Airport. This network has a dense core at the airport, consisting of 2 weather stations and 6 wind poles. Around the airport, 4 visibility stations and 4 KNMI automated weather stations (within 40 km distance of the airport) are included in the network. The average distance between neighbouring stations is 8.2 km.

Visual analysis shows that turbulent structures spanning multiple stations are found when using the Schiphol Airport network. With this discovery, the first research question (RQ 1) is answered. By comparing stations at increasing spatial separation, a first impression of the spatial scale of the structure is made. One example of a large structures shows a delayed and/or slightly different turbulent signal. While it is visually recognizable as the same turbulent event, a delayed turbulent signal between stations results in weak correlation. By applying the station correlation method, the resulting e-folding distances cases ranges between 1.4 km and 24.1 km, with a median of 8.9 km. Consequently, the answer to the second research question (RQ 2) is that the upper limit of the spatial scale of short-lived turbulent structures is estimated to be 8.9 km.

The e-folding distance consistently estimates the distance at which correlation becomes weak. For distances larger than the e-folding distance, a spread is found in the correlation coefficients, i.e. strongly and weakly correlated station pairs at similar distance. This spread is either caused by noise, or by an incorrect assumption of isotropy inherent to the method. The turbulent structures are often spatially anisotropic and the station correlation method consequently underestimates the scale of these structures. As a rule of thumb, the e-folding distance is comparable to the semi-minor axis of elliptical structures.

The large range of e-folding distances shows large variations between the different cases. It also gives valuable information the design of future networks to study short-lived turbulence. To capture larger structures as the ones studied here, it is recommended that such a network spans a minimum distance of 25 km. The smaller e-folding distances are of the same order of magnitude as the station distance at the airport. This indicates that the Schiphol Airport network is not sufficiently dense to analyze these small structures. It is therefore recommended that a future network includes a dense core, where observational stations are evenly spaced and where station distance is no larger than 1 km. Consistent spacing of the stations in the network is required to accurately capture the shape of the turbulent structure, as well as to study propagation. This recommendation answers the third and final research question (RQ 3).

In addition to turbulent structures, remarkable local variations in near-surface temperature are observed using the Schiphol Airport network. Local variations up to nearly $9^{o}C$, over distances of 40 km or less are found. During daytime these local variations typically remained less than $0.5^{o}C$, stressing the differences in atmospheric physics during day and night. Close to the runways of the airport, strong turbulence is observed which coincides with large airplanes taking off. This artificially created turbulence often increases the near-surface temperature with $4^{o}C$ in very short time. In spite of the short duration of take off, the increase in near-surface temperature, as compared to the background, remains present over a large time period (1 hour). It will be interesting to study the impact of artificial turbulence on the near-surface temperature as well, as a follow up of the current work.

# Acknowledgements

Bibliography

O. C. Acevedo, O. L. L. Moraes, G. A. Degrazia, and L. E. Medeiros. Intermittency and the Exchange of Scalars in the Nocturnal Surface Layer. *Boundary-Layer Meteorology*, 119:41–55, 2006. doi: 10.1007/s10546-005-9019-3.

C. Ansorge. *Analyses of Turbulence in the Neutrally and Stably Stratified Planetary Bounday Layer*. Springer International Publishing AG, 2016. ISBN 978-3-319-45043-8.

C. Ansorge and J. P. Mellado. Global Intermittency and Collapsing Turbulence in the Stratified Planetary Boundary Layer. *Boundary-Layer Meteorology*, 153:89–116, 2014. doi: 10.1007/s10546-014-9941-3.

A. K. Blackader. Boundary Layer Wind Maxima and Their Significance for the Growth of Nocturnal Inversions. *Bulletin American Meteorologocal Society*, 38(5):283–290, 1957.

R. L. Coulter and J. C. Doran. Spatial and Temporal Occurences of Intermittent Turbulence During CASES-99. *Boundary-Layer Meteorology*, 105:329–349, 2002. doi: 10.1023/A:1019993703820.

J. Donda. *Collapse of Turbulence in the Atmospheric Nocturnal Boundary Layer*. Eindhoven University of Technology, 2015. ISBN 978-90-386-3828-7.

P. He and S. Basu. Direct Numerical Simulation of Intermittent Turbulence under Stably Stratified Conditions. *Nonlinear Processes in Geophysics*, 22:447–471, 2015. doi: 10.5194/npg-22-447-2015.

A. Lapworth. The Evening Wind. *Weather*, 63(1):12–14, 2008. doi: 0.1002/wea.167.

L. Mahrt. Stratified Atmospheric Boundary Layers. *Boundary-Layer Meteorology*, 90:375–396, 1999.

L. Mahrt, J. Sun, W. Blumen, T. Delany, and S. Oncley. Nocturnal Boundary-Layer Regimes. *Boundary-Layer Mateorology*, 88:255–278, 1998.

D. Martínez, M. A. Jiménez, J. Cuxart, and L. Mahrt. Heterogeneous Nocturnal Cooling in a Large Basin Under Very Stable Conditions. *Boundary-Layer Meteorology*, 137:97–113, 2010. doi: 10.1007/s10546-010-9522-z.

A. F. Moene and J. C. Van Dam. *Transport in the Atmosphere-Vegetation-Soil Continuum*. Camebridge University Press, 2014. ISBN 978-0-521-19568-3.

A. H. Monahan, T. Rees, Y. He, and N. McFarlane. Multiple Regimes of Wind, Stratification, and Turbulence in the Stable Boundary Layer. *Journal of the Atmospheric Sciences*, 72:3178–3198, 2015. doi: 10.1175/JAS-D-14-0311.1.

P. Monti, H. J. S. Fernando, M. Princevac, W. C. Chan, T. A. Kowalewski, and E. R. Pardyjak. Observations of Flow and Turbulence in the Nocturnal Boundary Layer over a Slope. *Journal of the Atmospheric Sciences*, 59(17):2513–2534, 2002. doi: 10.1175/1520-0469.

R. Nakamura and L. Mahrt. A Study of Intermittent Turbulence with CASES-99 Tower Measurements. *Boundary-Layer Meteorology*, 114:367–387, 2005. doi: 10.1007/s10546-004-0857-1.

F. T. M. Nieuwstadt. The Turbulent Structure of the Stable Boundary Layer. *Journal of the Atmospheric Sciences*, 41(14):2202–2216, 1984. doi: 10.1175/1520-0469.

F. T. M. Nieuwstadt, J. Westerweel, and B. J. Boersma. *Turbulence. Introduction to Theory and Applications of Turbulent Flows*. Springer International Publishing, 1998. ISBN 978-3-319-31597-3.

O. Reynolds. On the Dynamical Theory of Incompressible Viscous Fluids and the Determination of the Criterion. *Phylosophical Transactions of Royal Society*, 186:123–191, 1895.

C. Román-Cascón, C. Yagüe, L. Mahrt, M. Sastre, G. J. Steeneveld, E. Pardyjak, A. Van de Boer, and O. Hartogensis. Interactions Among Drainage Flows, Gravity Waves and Turbulence: a BLLAST Case Study. *Atmospheric Chemistry and Physics*, 15:9031–9047, 2015. doi: 10.5194/acp-15-9031-2015.

J. A. Salmond. Wavelet Analysis of Intermittent Turbulence in a Very Stable Nocturnal Boundary Layer: Implications for the Vertical Mixing of Ozone. *Boundary-Layer Meteorology*, 114:463–488, 2005. doi: 10.1007/s10546-004-2422-3.

G. J. Steeneveld, S. Koopmans, B. G. Heusinkveld, L. W. A. Van Hove, and A. A. M. Holtslag. Quantifying Urban Heat Island Effects and Human Comfort for Cities of Variable Size and Urban Morphology in the Netherlands. *Journal of Geophysical Research*, 116:D20129–1–D20129–14, 2011. doi: 10.1029/2011JD015988.

R. B. Stull. *An Introduction to Boundary Layer Meteorology*. Kluwer Academic Publishers, 1988. ISBN 90-277-2768-6.

J. Sun, S. P. Burns, D. H. Lenschow, R. Banta, R. Coulter, S. Frasier, T. Ince, C. Nappo, J. Cuxart, W. Blumen, X. Lee, and X. Hu. Intermittent Turbulence Associated with a Density Current Passage in the Stable Boundary Layer. *Boundary-Layer Meteorology*, 105:199–219, 2002. doi: 10.1023/A:10199691317741.

J. Sun, S., L. Mahrt, R. Banta, and Y. L. Pichungina. Turbulence Regimes and Turbulence Intermittency in the Stable Boundary Layer during CASES-99. *Journal of Atmospheric Sciences*, 69:338–351, 2012. doi: 10.1175/JAS-D-11-082.1.

H. Tennekes and J. L. Lumley. *A First Course in Turbulence*. The MIT Press, 1972.

B. J. H. Van de Wiel. Transport processes in environmental science and engineering. Master Course, Delft University of Technology, 2016. Course code: CIE4701.

B. J. H. Van de Wiel, A. F. Moene, R. J. Ronda, H. A. R. De Bruin, and A. A. M. Holtslag. Intermittent Turbulence in the Stable Boundary Layer over Land. Part II: A System Dynamics Approach. *Journal of Atmospheric Siences*, 59(17):2567–2581, 2002a. doi: 10.1175/1520-0469.

B. J. H. Van de Wiel, R. J. Ronda, A. F. Moene, H. A. R. De Bruin, and A. A. M. Holtslag. Intermittent Turbulence in the Stable Boundary Layer over Land. Part I: A Bulk Model. *Journal of Atmospheric Siences*, 59(5):942–958, 2002b. doi: 10.1175/1520-0469.

B. J. H. Van de Wiel, A. F. Moene, O. K. Hartogensis, H. A. R. De Bruin, and A. A. M. Holtslag. Intermittent Turbulence in the Stable Boundary Layer over Land. Part III: A Classificaion for Observations During CASES-99. *Journal of Atmospheric Siences*, 60(20):2509–2522, 2003. doi: 10.1175/1520-046.

B. J. H. Van de Wiel, A. F. Moene, H. J. J. Jonker, P. Baas, S. Basu, J. M. M. Donda, J. Sun, and A. A. M. Holtslag. The Minimum Wind Speed for Sustainable Turbulence in the Nocturnal Boundary Layer. *Journal of Atmospheric Siences*, 69:3116–3127, 2012. doi: 10.1175/JAS-D-12-0107.1.

I. G. S. Van Hooijdonk, J. M. M. Donda, H. J. H. Clercx, F. C. Bosveld, and B. J. H. Van de Wiel. Shear Capacity as Prognistic for Nocturnal Boundary Layer Regimes. *Journal of Atmospheric Siences*, 72:1518–1532, 2015. doi: 10.1175/JAS-D-14-0140.1.

I. G. S. Van Hooijdonk, A. F. Moene, M. Scheffer, H. J. H. Clercx, and B. J. H. Van de Wiel. Early Warning Signals for Regime Transistion in the Stable Boundary Layer: A Model Study. *Boundary-Layer Meteorology*, 162:283–306, 2016. doi: 10.1007/s10546-016-0199-9.

A. H. Weber and R. J. Kurzeja. Nocturnal Planetary Boundary Layer Structure and Turbulence Episodes during the Project STABLE Field Program. *Journal of Applied Meteorology*, 30:1117–1133, 1991. doi: 10.1175/1520-0450.

J. C. Wyngaard. *Turbulence in the Atmosphere*. Cambridge University Press, 2010.

A
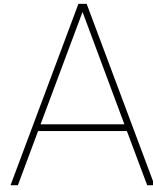
Schiphol Airport network

The Schiphol Airport network consists of a dense core of stations at the airport, four visibility stations around the airport and four AWS within a 40 km radius. The locations of all stations in the network are shown in figure 3.3. All observation locations are owned and maintained by the KNMI. This appendix discusses the stations at, and the visibility stations around, the airport in more detail.

At Schiphol Airport, there are two weather stations observing both temperature and wind speed. In addition, there are six wind poles at the airport, observing only wind speed. The stations at the airport are located at a minimum distance 105 m from the runways. Around the airport, at distances ranging from 7 km to 20 km, there are 4 visibility stations. These stations are mainly used for fog detection, but also observe temperature and wind speed.
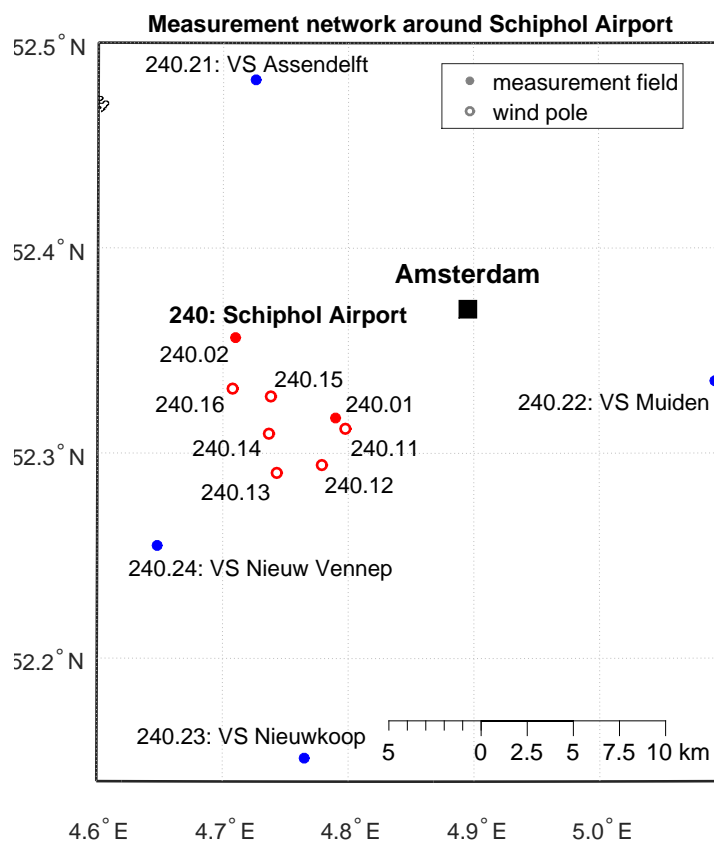

Figure A.1: The locations and station index of the stations in the observational network at Schiphol Airport. The stations shown as an empty circle only measure wind speed, while the other stations also measure the temperature at 0.1 and 1.5 m. Observations at the airport are shown in red and visibility stations at 7 to 20 km from the airport are shown in blue.

The stations in both the AWS network and the Schiphol Airport network are referred to with the letters "AWS", followed by the station index number. Schiphol Airport has station index 240, but there is no individual index for the individual stations in the network. This study uses decimals, in addition to the index 240, for all stations at Schiphol Airport. The two weather stations at the airport are referred to as AWS240.01 and AWS240.02. The six wind poles at the airport are referred to as AWS240.11 to AWS240.16. Finally, the four visibility stations are referred to as AWS240.21 to AWS240.24. The location of all stations, including their respective index, are shown in figure A.1. A highly detailed map of the airport and the location of the observational stations is found in figure A.2
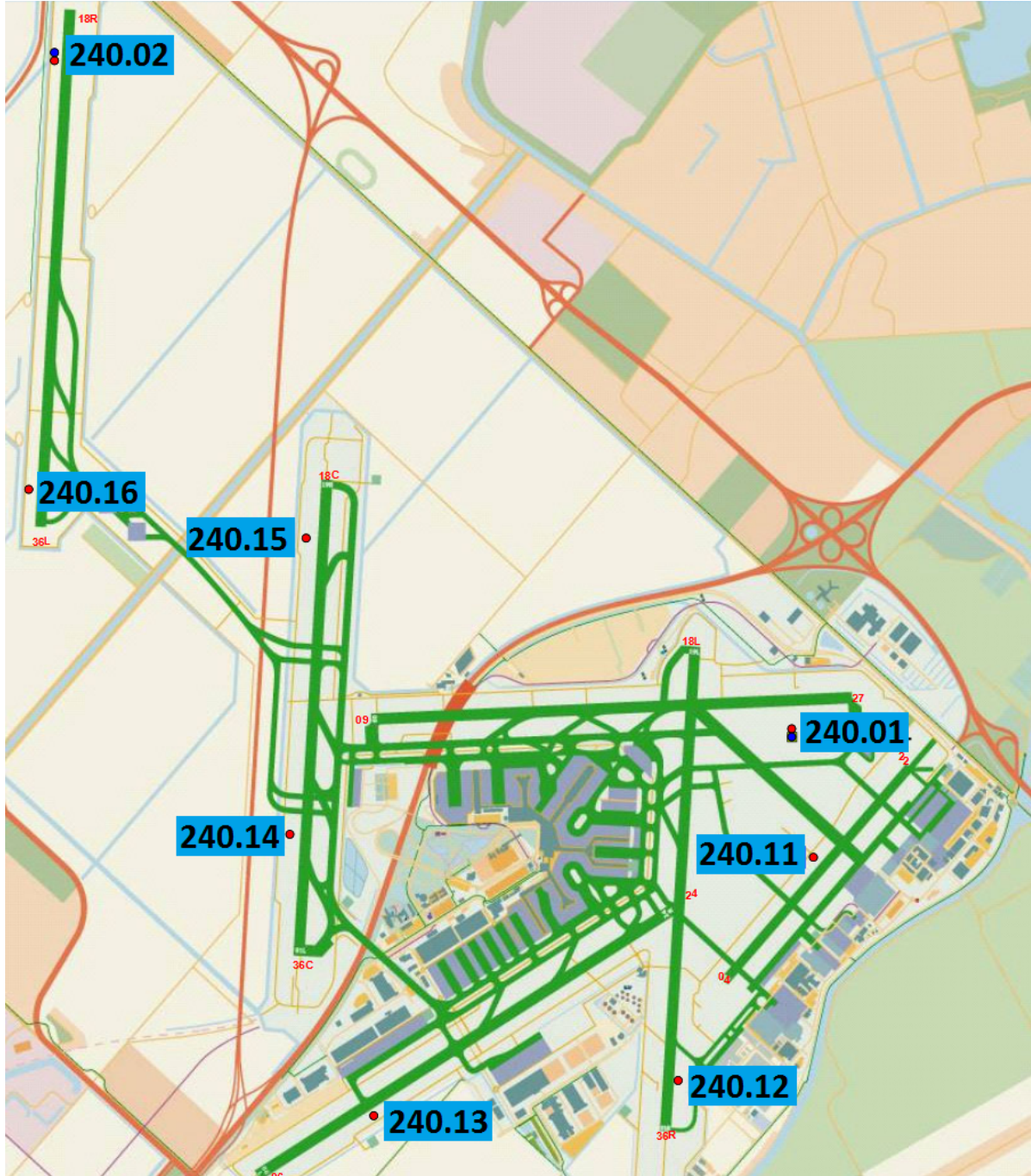

Figure A.2: A highly detailed map of the airport, including the locations of the observational stations. The stations are located at a minimum distance of 105 m from the runways. All stations observe u_{10m} and only AWS240.01 and AWS240.02 observe the temperature at 0.1 m and at 2 m.

Extraction of turbulent signals from observations

It is expected that there is some correlation between observations of wind speed and temperature for short-lived turbulent events. Two methods are developed to extract turbulent fluctuations from $T_{0.1m}$ and u_{10m} observations. This section discusses these two methods and their effectiveness.

The first method subtracts a weightless moving average with a 190 minute window from both observations (section 3.4). The remaining fluctuations, $MATF$ and $MAWF$, are considered as the turbulent signal. The second method is based on the theory that a short-lived increase in wind speed (turbulence) results in a short-lived increase in near-surface temperature. It assumes that the u_{10m} observations is the turbulent signal and
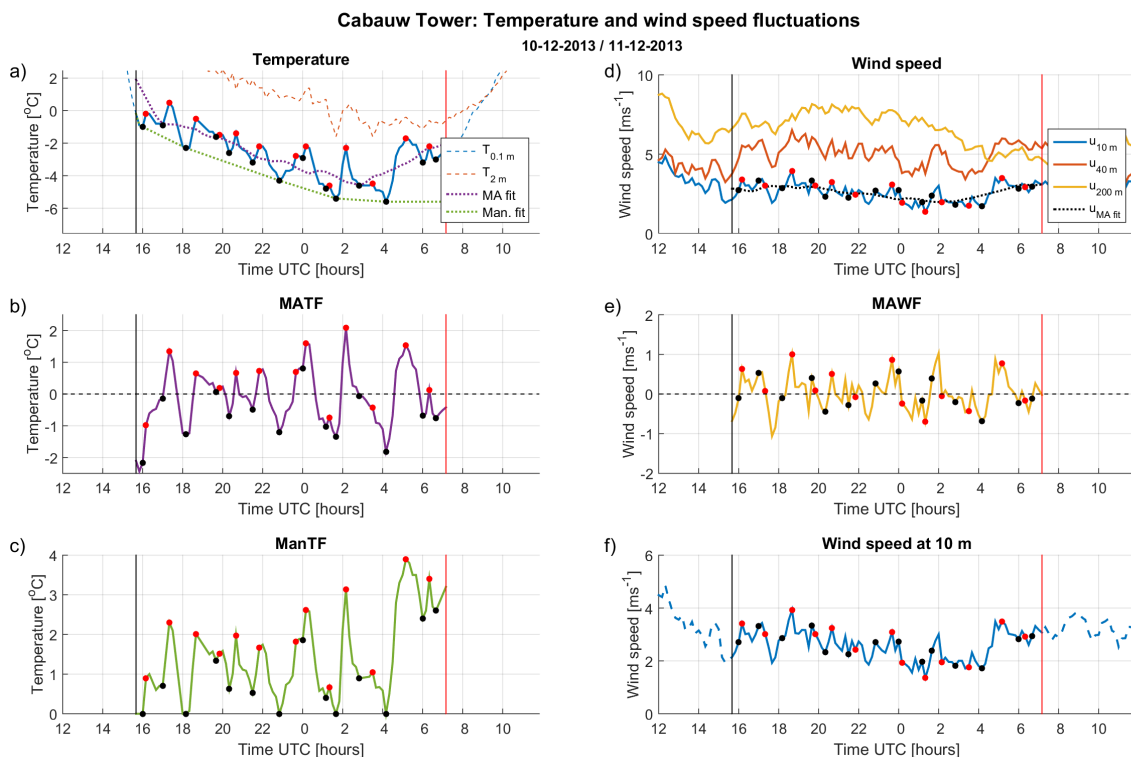

Figure B.1: Turbulent fluctuations, extracted from observations of temperature and wind speed. $T_{0.1m}$ observations, as well as the moving average fit (purple) and the manual fit (green) are shown in a. The $MATF$ and the $ManTF$ are shown in b and c respectively. Wind speed observations, including the moving average fit, are shwon in d. The $MAWF$ and u_{10m} observations are shown in e and f respectively. The correlation between the signals in the left and right panel of the second level (b and e) will be studied. The correlation between the signals in the left and right panel of the third level (c and f) will also be studied.
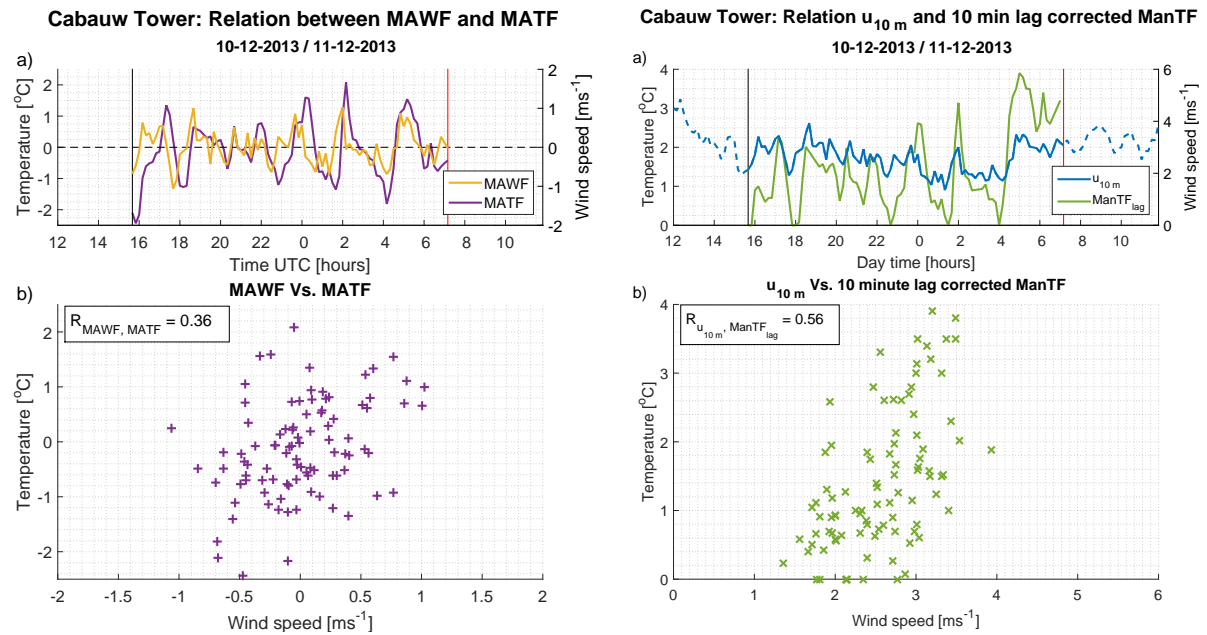
Figure B.2: Two time series of the $MATF$ (purple) and the $MAWF$ (yellow) are shown in a. The image shows that the two signals are very similar and that they therefore are related. A scatter diagram of the $MAWF$ against the $MATF$ is shown in b. When there is a strong relation between the two parameters, a linear relation should be visible in this image. The relation is quantified by a correlation coefficient $R_{MAWF,MATF}$ of 0.36 in the top left of the image. The image in c is similar to a, but now comparing the $ManTF$ (green) with the u_{10m} observations (blue). This image indicates some coherence between the two signals, but it is not as clear as in a. Image d is similar to image b, but shows the correlation between $ManTF$ and the u_{10m} observations. This scatter diagram shows a stronger linear pattern than what was found in b. The $R_{ManTF,u}$ is also significantly higher with a value of 0.56.

that only $T_{0.1m}$ fluctuations need to be extracted. This is done by subtracting a manual fit (Man) from the observations.

The manual temperature fit attempts to estimate the effect of radiative cooling on near-surface temperature in order to extract temperature fluctuations from the observations. It is based on an automated fit that follows the observations as long as $T_{0.1m}$ is lower than the previous moment in time. If this is not the case, it will maintain a constant temperature until $T_{0.1m}$ decreases again. This automatic fit can be altered manually. The user can manually overwrite the fit and draw a straight line form one local minimum to another. When this manual fit is subtracted, the remaining manual temperature fluctuations ($ManTF$) are assumed the turbulent signal.

The effectiveness of the methods depends partly on the correlation between the wind speed and temperature signal of turbulence. When the correlation is high, it is assumed that turbulence is captured well. An example of the temperature and wind signals of both methods, as well as the original observations, is shown in figure B.1. The original temperature and wind speed observations, as well as the the fits, are shown in figure B.1a and d respectively. The remaining panels in the figure show the turbulent signals. The correlation coefficient between both the $MATF$ (figure B.1b) and $MAWF$ (figure B.1e) signals ($R_{MAWF,MATF}$), as well as between the $ManTF$ (figure B.1c) and u_{10m} (figure B.1f) observations ($R_{ManTF,u}$) are studied for the example of figure B.1.

A visual comparison of the $MATF$ and the $MAWF$, shown in figure B.2a and already discussed in section 3.4, show strong coherence and a short time delay. The visual comparison of the $ManTF$ and the u_{10m} observations show poorer coherence. The correlation coefficient $R_{MAWF,MATF}$ is only 0.36, where the correlation coefficient $R_{ManTF,u}$ is 0.56. The other cases generally also show a higher correlation between the $ManTF$ and the u_{10m} observations, than between the $MATF$ and $MAWF$ signals. The correlation coefficients of both methods are found in table B.1.

While the manual fit method is shown to be an effective method to extract the turbulent signal from observations, it has disadvantages. The manual fit procedure is time consuming and has a strong subjective element. This can become a complicated process when studying multiple stations. An automated process is

Table B.1: The correlation coefficients of the two methods used to extract turbulent signals from observations. The correlation coefficients of the manual fit method are shown in the first column. The correlation coefficients of the moving average fit method are shown in the second column. The third column shows the time delay corrected correlation coefficients.

Dates	$R_{ManWF,ManTF}$ []	$R_{MAWF,MATF}$ []	$R_{MAWF,correctedMATF}$ []
10-12-2013 to 11-12-2013	0.56	0.36	0.66
11-09-2014 to 12-09-2014	0.78	0.74	0.82
15-02-2015 to 16-02-2015	0.71	0.62	0.74
14-04-2015 to 15-04-2013	0.91	0.67	0.83
17-04-2015 to 18-04-2005	0.13	0.35	0.71
01-10-2015 to 02-10-2015	0.63	0.29	0.63
16-03-2016 to 17-03-2016	0.87	0.65	0.80

therefore preferred. Therefore, the moving average method is studied further by considering the time delay that was found in figure B.2a.

When the time delay is corrected for, as described in section 3.4, $R_{MAWF,correctedMATF}$ increases significantly. The delay corrected correlation coefficients for all 7 cases are shown in the third column of table B.1. This table shows that $R_{MAWF,correctedMATF}$ is significantly high for all cases and sometime outperforms $R_{ManTF,u}$. This shows that the automated moving average method captures the turbulent signals accurately. Moving average fluctuations are used when studying short-lived turbulence using the observations from the networks, because turbulence is captured well and because of the advantages of an automated method.
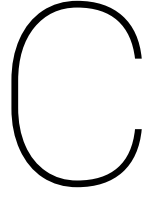
The e-folding distance

The e-folding distance is used in station correlation method to estimate the spatial scale of short-lived turbulent structures (3.5). In science, e-folding is a characteristic variable concerning exponential growth/decay of a quantity. In this Appendix, the principle of e-folding is discussed based on exponential decay.

Generally, e-folding refers to the e-folding time, which is the time it takes for a quantity to be decrease to $1/e$, i.e. 0.368, of its previous value. It is a characteristic time of an exponentially decaying function. The principles of the e-folding time are the same to that of the better known half-life. The latter describes the time it takes for a exponentially decaying quantity to reach half its original value. The half-life is best known for its use in radioactive decay.

When e-folding is applied to study the spatial scale of short-lived turbulence, the correlation coefficient between two stations is the aforementioned quantity which expected to decay exponentially with distance. As a consequence, the e-folding distance is used.

The station correlation method applies an exponentially decaying fit to the scatter diagram, which relates distance between stations to the correlation coefficient between those pairs of stations. The decaying exponential is shown in equation 3.2 and repeated below,

$$R(d) = e^{-x/C}, \tag{C.1}$$

where R is the correlation coefficient, x is the distance between two stations and C is a constant describing the rate of decay. The original correlation coefficient, i.e. at $x = 0$ km, is equal to one. The e-folding distance therefore describes the distance at which the correlation coefficient of the exponential fit is equal to $1/e$.

In this study, the e-folding distance is defined as the distance at which stations do not experience a specific turbulent structures, i.e. the stations are not significantly correlated. It is a more or less objective estimate of the distance at which correlation becomes weak. The e-folding distance (δ) of equation C.1 is equal to constant C as proven below:

$$e^{-\delta/C} = 1/e,$$
$$-\delta/C = -1,$$
$$\delta = C.$$

It is this constant C that is estimated using non-linear least squares in the station correlation, when applying the fit to the data in the scatter diagram.

A remarkable characteristic of the e-folding distance is that the surface area underneath the exponential fit is equal to the surface area of a rectangle, with its base on the x-axis, between $x = 0$ and $x = \delta$, and a height 1 (the original value of the correlation coefficient), which has a surface area of δ times 1. This is proven by:

$$\int_0^\infty e^{-x/\delta} dx = \left[-\delta e^{-x/\delta} \right]_0^\infty,$$
$$\int_0^\infty e^{-x/\delta} dx = 0 - (-\delta) = \delta.$$

D

Additional exemplary cases of the Schiphol Airport network

Two of examples, out of the eleven cases that were studied using the Schiphol Airport network, are discussed in detail in chapter 5. This appendix provides two more example cases. The first case, the night of the 23th and 24th of March 2015, is an example of a turbulent structure which is more or less spatially isotropic. The second case, the night of the 12th and 13th of April 2016, is a structure which is clearly spatially anisotropic.

The two cases are not discussed in detail. They serve as additional examples to display the effect of the assumption of spatial isotropy in the station correlation method. For each case, the near-surface temperature and wind speed time series are shown, as well as the scatter diagram of the station correlation method and a correlation map.
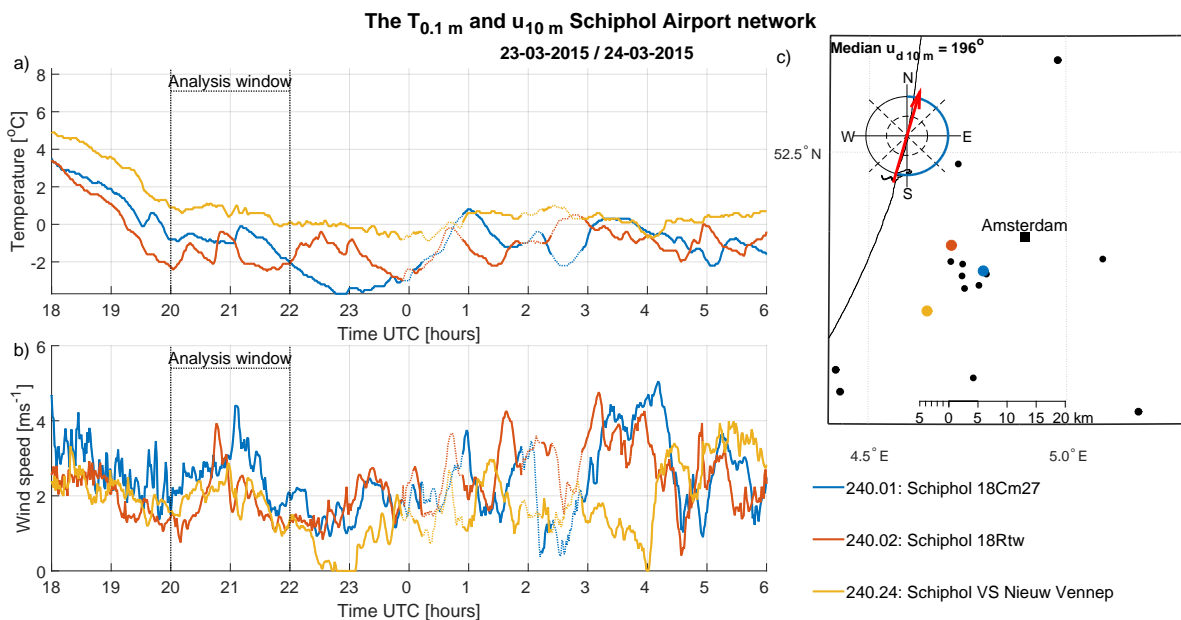

Figure D.1: The $T_{0.1m}$ (a) and u_{10m} (b) observations on the night of the 23th and 24th of March 2015, as well as the location of the AWS with the median u_{d10m} at the airport (c). The time series of the turbulent event is shown in the analysis window. A clear turbulent event is found at AWS240.01 and AWS240.02, be it with small differences in characteristics. AWS240.24 observes a weak turbulent event as well. At both AWS240.01 and AWS240.02, $T_{0.1m}$ increases nearly simultaneous with u_{10m}. The $T_{0.1m}$ at AWS204.24 shows a weak response ($< 2^oC$) to the weak turbulent event.
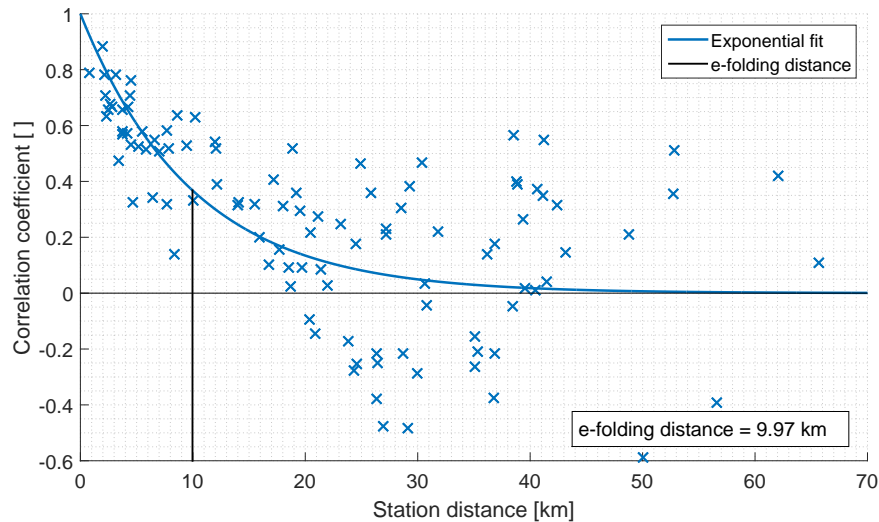
Figure D.2: The results of the station correlation method of the night of the 23th and 24th of March 2015. It shows a scatter diagram of the station distance against the correlation coefficient of the time series within the analysis window between all station combinations. An exponential fit to the data is shown in blue. The e-folding distance (black) is used to estimate of the spatial scale of the structure to be 10.0 km.

The time series of the $T_{0.1m}$ (a) and u_{10m} (b) observations and the locations of the three stations on the map (c) are shown for the first case in figure D.1. A clear short-lived turbulent event is observed within the analysis window at AWS240.01 and AWS240.02. The u_{d10m} (not shown) changes from approximately 250° to 150° between 18:00 and 0:00 UTC. The median u_{d10m} of the analysis window time series being 196° (figure D.1c). Events outside the analysis window are not part of that turbulent event and are not considered in the station correlation method.

The scatter diagram, resulting from the station correlation method, relates station distance to the correlation coefficient, as shown in figure D.2. An exponential fit (according to equation 3.2) is made to the data in the diagram, as can be seen in the figure. The residuals to this fit are small until a distance of approximately 15 km. This indicates that the assumption of spatial isotropy of the structure is more or less valid. The spatial scale of this short-lived turbulent structure, estimated by the e-folding distance, is 10.0 km. Stations at distances larger than the e-folding distance

The validity of the assumption of spatial isotropy in the station correlation method is studied using a correlation map, shown in figure D.3. This map shows the correlation from 0 (white) to 1 (red) between all stations and the reference station AWS240.14 (solid black). Linear interpolation is used between the stations. This map shows that high correlation ($R > 0.5$) is found between all stations at the airport, as well as with AWS240.24, just southeast of the airport. Weak and moderate correlation is found north and west of the airport. Correlation with stations east of the airport is weak.

The linear interpolation in the correlation map of figure D.3, suggest an elongated shape of the structure. However, no proof of this is found in the correlation at the stations in figure D.3, nor in the scatter diagram of figure D.2. Due to the limitations of the Schiphol Airport network (discussed in section 5.1.2) however, no definitive conclusion can be drawn about the shape of the structure. The data presented indicate that, for this turbulent structure, the assumption of spatial isotropy is valid.
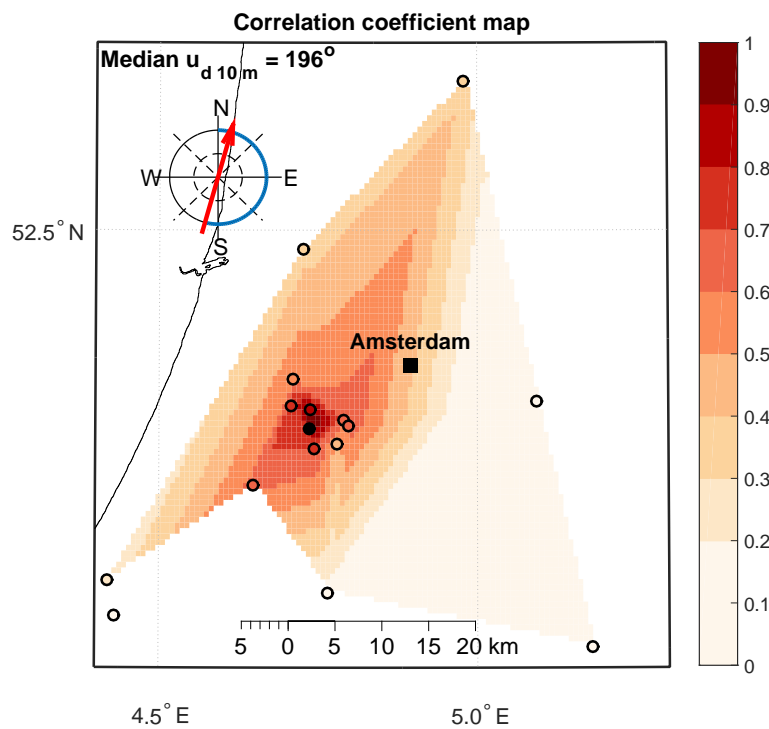
Figure D.3: The correlation coefficients between AWD240.14 and the other stations in the Schiphol Airport network, on the night of the 23th and 24th of March 2015. Significant correlation is found with the stations at the airport, as well as with AWS240,24, located south-southwest of the airport.
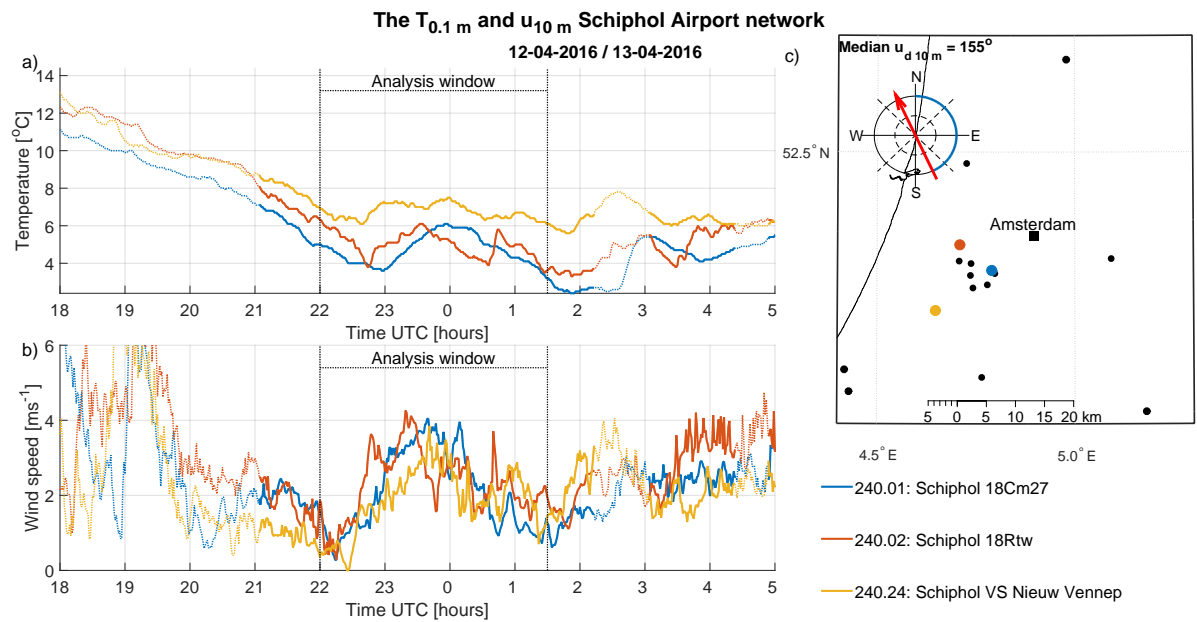
Figure D.4: The $T_{0.1m}$ (a) and u_{10m} (b) observations on the night of the 12th and 13th of April 2016, as well as the location of the AWS with the median u_{d10m} at the airport (c). The time series of the turbulent event is shown in the analysis window. A clear turbulent event is found at all three stations, be it with minor differences in characteristics. $T_{0.1m}$ increases near simultaneous with u_{10m} at AWS204.01 and AWS240.02. A weaker response ($< 2^oC$) in $T_{0.1m}$ is found at AWS240.24.

The time series of the $T_{0.1m}$ (a) and u_{10m} (b) observations and the locations of the three stations on the map (c) are shown for the second case in figure D.4. A clear short-lived turbulent event is observed within the analysis window at all three stations. Events outside the analysis window are not part of that turbulent event and are not considered in the station correlation method.

The scatter diagram for this turbulent event, resulting from the station correlation method, us shown in figure D.5. The residuals to the exponential fit (blue) are relatively large and increase with distance, until about 30 km. Between about 15 km and 30 km, a large spread in the data is found. Both high and (negative) low correlation is found here. This indicates that the assumption of spatial isotropy of the structure invalid. Similar to other cases, the e-folding distance (black) estimates the distance at which the first few weakly correlated pairs of stations are found. Using the e-folding distance, the spatial scale of the structure is estimated at 15.4 km.

The validity of the assumption of spatial isotropy in the station correlation method is studied using the correlation map of figure D.6. This map shows that high correlation ($R > 0.5$) is found between all stations at the airport, as well as with the stations south and southwest of the airport. Stations north and east of the airport are weakly correlated with the reference stations AWS240.14. This map shows that the assumption of spatial isotropy is invalid for this structure and that both distance and direction determine the correlation between stations.

The map in figure D.6 also shows that the scale estimation by the e-folding distance is an underestimation. AWS210 (southwest of the airport) and AWE240.23 (south of the airport) are highly correlated with the reference station (AWS240.14), located at about 30 km and 20 km distance. Assuming an elliptical structure, the e-folding distance seems to correspond to the semi-minor axis of the structure. Similar results to this are found in other cases (section 5.1.2). When the assumption of spatial isotropy is invalid, the station correlation underestimates the spatial scale of short-lived turbulent structures.
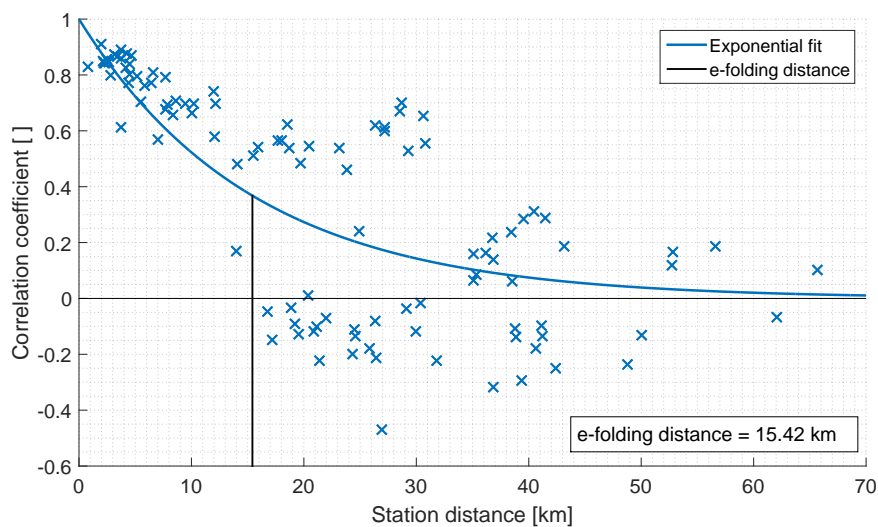
Figure D.5: The results of the station correlation method of the night of the 12th and 13th of April 2016. It shows a scatter diagram of the station distance against the correlation coefficient of the time series within the analysis window between all station combinations. An exponential fit to the data is shown in blue. The e-folding distance (black) is used to estimate of the spatial scale of the structure to be 15.4 km.
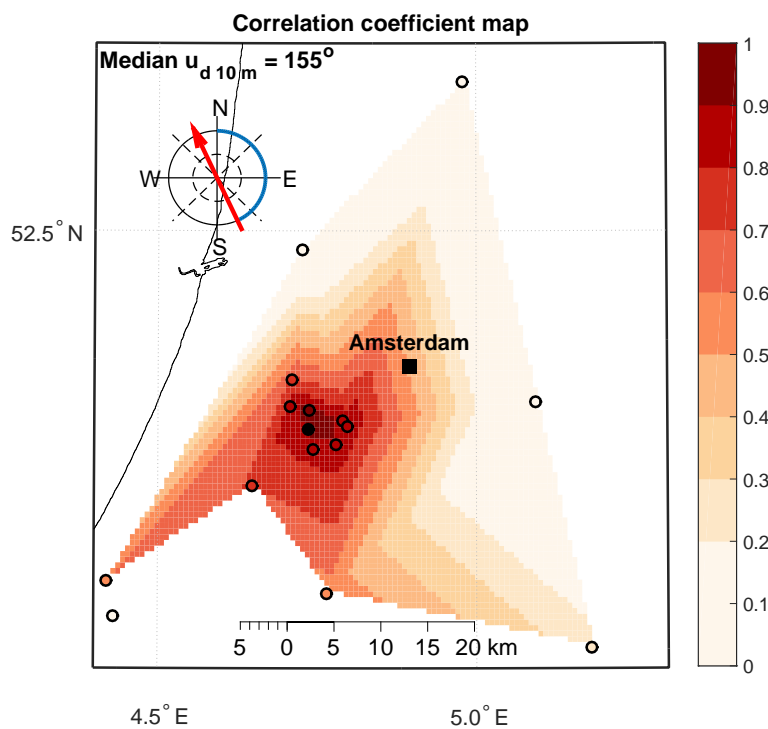

Figure D.6: The correlation coefficients between AWD240.14 and the other stations in the Schiphol Airport network, on the night of the 12th and 13th of April 2016. Significant correlation is found with the stations at the airport, as well as with stations south and southwest of the airport. Weak correlation is found north and east of the airport.